minerals

MDPI

Article

Early Cretaceous Granitoids Magmatism in the Nagqu Area, Northern Tibet: Constraints on the Timing of the Lhasa–Qiangtang Collision

Kaiyang Wu [1], Yun Zhong [2], Yajuan Yuan [1,*], Zhifeng Wan [3], Bin Xia [3] and Tengfei Wu [4]

[1] School of Geography, South China Normal University, Guangzhou 510631, China; wuky@m.scnu.edu.cn
[2] School of Surveying and Mapping, Guangdong Polytechnic of Industry and Commerce, Guangzhou 510510, China; cloudzj@gdgm.edu.cn
[3] School of Marine Sciences, Sun Yat-sen University, Zhuhai 519082, China; wanzhif@mail.sysu.edu.cn (Z.W.); xiabin@mail.sysu.edu.cn (B.X.)
[4] Oklahoma Geological Survey, Norman, OK 73019, USA; victorwu@ou.edu
* Correspondence: yuanyajuan@m.scnu.edu.cn

Abstract: The timing of the Lhasa–Qiangtang collision following the closure of the Bangong–Nujiang Tethys Ocean has not been well constrained. An integrated study of whole-rock geochemistry and zircon U–Pb–Hf isotopes was carried out for Early Cretaceous quartz diorite-porphyrites and granites from the Yilashan and Amdo areas, northern Tibet. LA–ICP–MS zircon U–Pb dating reveal that the Yilashan and Amdo granitoids were emplaced at ~121–110 Ma. These granitic rocks display selective enrichment of light rare earth elements, large ion lithophile elements (e.g., Rb, U) and Th, but depletion of Sr and high field strength elements (e.g., Nb, Ta, Ti) compared to its neighboring elements. These new data, combined with regional geological setting, show that these igneous rocks were formed under a geodynamic setting of the Lhasa and Qiangtang (–Amdo) collision with oceanic slab breakoff and asthenospheric upwelling. The BNTO had been closed at ~121–110 Ma in the study area. Yilashan-Amdo granitoids roughly yield high $(^{87}Sr/^{86}Sr)_i$ ratios and obvious negative $\varepsilon_{Nd}(t)$ and zircon $\varepsilon_{Hf}(t)$ values along with old Nd T_{DM} and zircon Hf T_{DM2} ages. Together with their variable U–Pb ages, these features indicate a Precambrian "hidden" crustal source beneath the northern Lhasa and Amdo terranes. The YLSS S-type granophyres were derived from partial melting of Paleoproterozoic lower crustal metagraywackes, whereas the YLSZ quartz diorite–porphyrites and the Amdo I- and A-type granites were mainly derived from partial melting of Paleo–Mesoproterozoic lower crustal mafic rocks with a certain amount of addition of mantle-derived melts. Minor amounts of the materials originated from the Amdo orthogneisses may also be involved in the formation of the YLSZ quartz diorite–porphyrites and the Amdo I-type granites. In addition, the Yilashan ophiolite was intruded by the ~112–108 Ma granophyric and quartz diorite–porphyritic intrusions before its final emplacement into the surrounding strata.

Keywords: granitoid; geochemistry; zircon U–Pb dating; continental–continental collision; Bangong–Nujiang suture zone

Citation: Wu, K.; Zhong, Y.; Yuan, Y.; Wan, Z.; Xia, B.; Wu, T. Early Cretaceous Granitoids Magmatism in the Nagqu Area, Northern Tibet: Constraints on the Timing of the Lhasa–Qiangtang Collision. *Minerals* **2022**, *12*, 933. https://doi.org/10.3390/min12080933

Academic Editor: Jaroslav Dostal

Received: 17 June 2022
Accepted: 22 July 2022
Published: 24 July 2022

1. Introduction

As the widest distribution rocks in continental crust, granitoids have attracted considerable interest due to their indicative petrogenesis and tectonic implications, such as the reworking of continental crust and the regional tectonic evolution and geodynamics [1–6]. It is well known that granitoids expose widely in the Tibetan Plateau and were generally produced associated with the closure of Tethyan and subsequent collisional orogeny over geological periods [7–11]. The studies of these rocks could be useful for constraining the formation and evolution and geodynamics process of the Tibetan Plateau.

The Bangong–Nujiang suture zone (BNSZ), a nearly E–W extending tectonic belt located between the Lhasa and southern Qiangtang terranes in the northern Tibet, represents the now-vanished Bangong–Nujiang Tethys Ocean (BNTO) and is one of the most important suture zones in the Tibetan Plateau (Figure 1a,b). Although many studies of ophiolites or ophiolitic complexes, which are discontinuously distributed in the BNSZ, have been done, the tectonic evolution of the BNSZ are still not well constrained. Especially compared with the India–Asia collision zone, the timing of the Lhasa–Qiangtang collision following the closure of the BNTO and the associated magmatic process remains inadequately understood. Integrated studies, including sedimentation transition, foreland basin system, structural patterns, igneous rocks and paleomagnetism, show that the closure time of the BNTO may be Middle Jurassic [12,13], Late Jurassic–Early Cretaceous (the main point of view is Early Cretaceous [14–24]) or after the Late Early Cretaceous [25–30]. Moreover, some workers suggested that the BNTO has a scissor-like diachronous closure and collision model along the strike that roughly began from Early Cretaceous in the east to Late Cretaceous in the middle-west according to the evidences of sedimentary and igneous rocks [31,32].

Mesozoic granitoids expose widely along the middle part of the BNSZ (Figure 1b); the studies of these rocks can provide a means to understand the closure of the BNTO and ultimate collisional orogeny. The Amdo terrane is a striking microcontinent sandwiched between the southern Qiangtang and Lhasa blocks, which occurs near the central BNSZ (Figure 1b). The remarkable ancient metamorphic basement intruded by abundant Mesozoic granitoids of this terrane make the Amdo terrane a critical area along the BNSZ to decipher the geological history of the BNSZ and northern Tibet [12,33–35]. However, previous studies were mainly conducted on metamorphic rocks of this terrane [12,36–41]. Relatively less attention has been given to the genesis and implications of the Mesozoic granitoids exposed in this terrane, especially the genetic types, while magma sources and the evolution of these Early Cretaceous granitoids have not yet been fully answered [8,11,12,37,42]. On the other hand, the Yilashan ophiolite is a well-known ophiolite in the central BNSZ (Figure 1b), and several studies about its geochronology and petrogenesis to constrain the tectonic evolution of the BNTO have been reported. In contrast to mafic–ultramafic rocks, few studies have focused on the origin and evolution of the granophyric and quartz diorite–porphyritic intrusions in the Yilashan ophiolite (Figure 2a–c). However, their genesis and formation age will be very helpful for studying the tectonic evolution of the Yilashan ophiolite, such as the formation and tectonic emplacement ages of the Yilashan ophiolite, which have not been well or direct defined yet [43–46].

In this paper, detailed whole-rock geochemical, geochronological and Sr–Nd–Hf isotopic data of the granophyric and quartz diorite–porphyritic intrusions in the Yilashan ophiolite and the Early Cretaceous granites (BCD, BCN, TL) distributed in the Amdo terrane (Figures 1 and 2) are presented. Based on these results and previous studies, we aim to determine the petrogenesis, tectonic setting and formation age of these rocks and then to constrain the closure of the BNTO and subsequent Lhasa–Qiangtang collision.

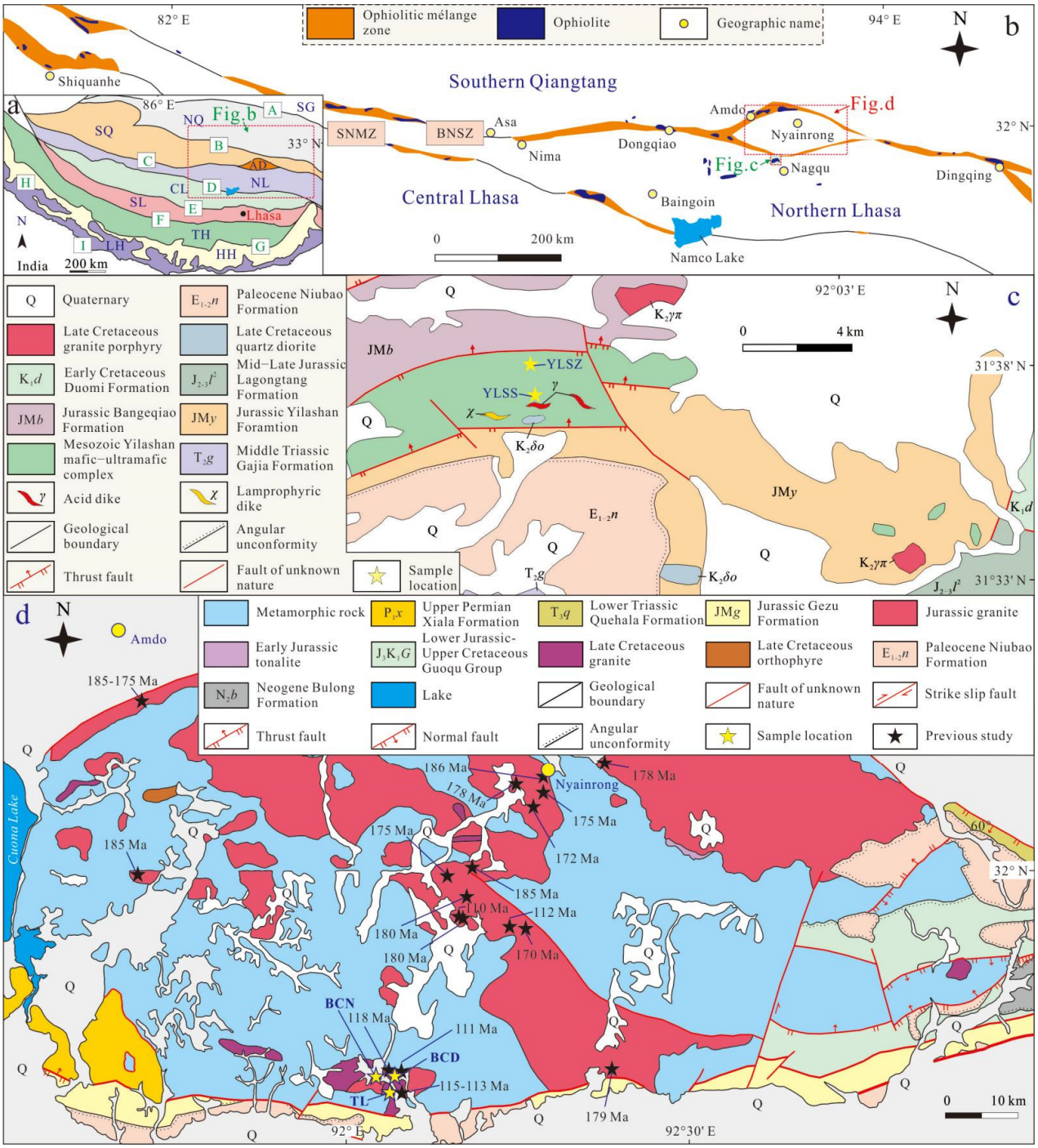

Figure 1. Inset showing the location of Figure 1b in the Tibetan Plateau (**a**) [9]. SG: Songpan–Ganzi terrane; NQ: Northern Qiangtang terrane; SQ: Southern Qiangtang terrane; AD: Amdo terrane; NL: Northern Lhasa terrane; CL: Central Lhasa terrane; SL: Southern Lhasa terrane; TH: Tethyan Himalaya terrane; HH: High Himalaya terrane; LH: Lesser Himalaya terrane. A: Jinsha suture zone; B: Longmuco–Shuanghu suture zone; C: Bangong–Nujiang suture zone; D: Shiquanhe–Namco mélange zone; E: Luobadui–Milashan fault; F: Yarlung Zangbo suture zone; G: South Tibetan detachment system; H: Main boundary trust; I: Main boundary trust. Tectonic outline of the Tibetan Plateau and the sketch structural framework of the Lhasa–southern Qiangtang terranes showing the Bangong–Nujiang suture zone (**b**) [9]. Geological sketch maps of the Yilashan ophiolite (**c**) [33] and the Amdo terrane (**d**) [33,34] showing sample localities.

Figure 2. Field photographs of the Yilashan and Amdo granitoids in the Nagqu area. (**a**) YLSS granophyre; (**b**) YLSZ quartz diorite–porphyrite; (**c**) Peridotite intruded by the YLSZ quartz diorite–porphyrite; (**d**–**f**) Amdo BCD, BCN and TL granites.

2. Geological Background

The Tibetan Plateau, western China (Figure 1b), the newest, highest and largest continental plateau on Earth, is marked by a series of exotic terranes including the Qaidam, Songpan–Ganzi, Qiangtang, Lhasa and Himalaya blocks from north to south, and these

fragments are separated by the Kunlun, Jinshajiang, Bangong–Nujiang and Yarlung Zangbo suture zones from north to south, respectively (Figure 1a) [31]. The Qiangtang and Lhasa blocks were separated from Gondwana and accreted to the southern margin of Eurasia in the late Paleozoic–Mesozoic [47,48]. Generally, the Qiangtang terrane is divided into northern and southern parts by the Longmuco–Shuanghu suture zone, and the Lhasa terrane is composed of northern, central and southern parts separated by the Shiquanhe–Namco mélange zone and Luobadui–Milashan Fault (Figure 1a) [7,49]. The southern Qiangtang terrane is dominated by Ordovician–Cretaceous marine and continental sedimentary rocks and Late Carboniferous–Paleogene igneous rocks [9,49–52]. A series of Mesozoic igneous rocks including mafic–felsic volcanic and granitic rocks are exposed along the southern margin of the southern Qiangtang terrane and were likely formed related to the northward subduction of the BNTO underneath the Qiangtang terrane [11,15,26,53]. In addition, the Lhasa terrane mainly consists of Paleozoic–Mesozoic continental–marine sediments and Mesozoic–Cenozoic igneous rocks with local Archean–Proterozoic metamorphic rocks [8,10,18,54,55]. That is, the northern and southern Lhasa blocks roughly exhibit juvenile crust affinities related to the subduction of Tethys Ocean and the central Lhasa block occurs with a Precambrian metamorphic crystalline basement that was once to be an ancient microcontinent [7,8,52,56].

The BNSZ is nearly 2000 km long and 20–200 km wide from west to east and contains abundant ophiolites or ophiolitic mélanges (Figure 1b,c) [57]. Previous studies revealed that these rocks roughly display two types of geochemical compositions including MORB (mid-ocean ridge basalt)-like and dominated SSZ (supra-subduction zone)-like components, and were mainly generated during the Early Jurassic–Early Cretaceous [17,44,45,58–60]. Namely, the BNTO had experienced a long tectonic history before the southern Qiangtang and Lhasa collision during the Early Cretaceous. In addition, a series of Mesozoic magmatic rocks exposed at the northern Lhasa terrane, the Amdo terrane and the southern margin of the southern Qiangtang terrane, reveal the likely bidirectional subduction of the BNTO in a N–S direction during this time [7–9,18,61].

The Yilashan ophiolite is exposed at the northern Lhasa terrane adjacent to the Amdo terrane, nearly 20 km NW of Nagqu city (Figure 1c). It occurs with an approximate rhombic shape, is nearly 13 km long and 3 km wide and contacts with the Jurassic Mugagangri Group (JM*b* and JM*y*; accretionary complex) by thrust faults on both the north and south sides (Figure 1d) [33]. There are reported three zircon LA–ICP–MS U–Pb ages of 169.6 ± 3.3, 132.5 ± 2.5 and 133.6 ± 4.9 Ma for diabases [45]. Again, two zircon LA–ICP–MS U–Pb ages of 183.7 ± 1 Ma and 162.8 ± 3.0 Ma for gabbro were reported by [43,46], respectively. Thus, the Yilashan ophiolite was likely formed in the Early Jurassic–Early Cretaceous. The Yilashan ophiolite is usually considered to be generated in an SSZ-related setting [43]. In addition, intermediate–felsic intrusions, such as granophyre, quartz diorite–porphyrite and lamprophyre, distribute locally within the Yilashan ophiolite (Figures 1d and 2a–c) [33].

The Amdo terrane contains foliated orthogneiss with subordinate granulite, paragneiss, amphibolite, and migmatite and sedimentary and metasedimentary rocks (Figure 1c) [12,35–40,62]. The orthogneisses contain intermediated–felsic rocks with their protoliths commonly being granites and granodiorites. It shows a bimodal crystallization age distribution of Neoproterozoic (~920–820 Ma) and Cambrian–Ordovician (~550–420 Ma), and then were metamorphosed at ~190–169 Ma [12,35,37,39–41]. Furthermore, the Amdo terrane was intruded by abundant and commonly undeformed Mesozoic granitoids (Figures 1b and 2d–f) [7,8,11,33,34,42]. These granitoids consist of granite, monzonite, granodiorite, syenite, tonalite and diorite, and roughly belong to the peraluminous calc–alkaline–shoshonite series [8,11] and were developed in two episodes with a major one of ~186–170 Ma and a minor one of ~140–100 Ma [8,11,12,42]. In addition, the Amdo terrane may not be a part of the Lhasa or Qiangtang terranes due to a different metamorphic crystalline basement from those of the latter two [8,12,35,39,51]. It was possibly an isolated microcontinent in the BNTO during the Permian to Triassic [8,9,35,41,62], and ultimately collided with the southern Qiangtang terrane [41] or subducted beneath the Amdo intra-

oceanic back-arc basin [17] in the Early Jurassic associated with the northward subduction of the BNTO, which triggered the Early Jurassic (~186–170 Ma) granitic magmatism and coeval high-pressure metamorphism (~190–169 Ma) in the Amdo terrane prior to the Lhasa and Qiangtang (–Amdo) collision during the Early Cretaceous [11,35,37,38,40–42,63,64].

3. Petrography

The YLSS coarse-grained granophyres display a porphyritic texture with clear quartz (20%–30%) and plagioclase (40%–45%) phenocrysts (Figure 3a). Plagioclase had undergone various degrees of sericitization and muscovitization. Granophyric K–feldspar and quartz with graphic–myrmekitic textures are common around the plagioclase and quartz phenocrysts. The matrix mainly consists of quartz and feldspar along with a small amount of inter-filled biotite and muscovite.

The YLSZ quartz diorite–porphyrites have a porphyritic texture and the phenocrysts mainly comprise hornblende (~5%), plagioclase (20%–25%) and quartz (~20%) (Figure 3b). Hornblende had experienced variable degrees of chloritization and epidotization, and plagioclase was altered by some degree of carbonatation and epidotization. The matrix is mainly composed of plagioclase, quartz, epidote and hornblende along with some inter–filled epidote, carbonate and chlorite.

The BCD granites are fine-grained allanite–biotite granites, which consist of K–feldspar (30%–40%), plagioclase (25%–35%), quartz (20%–30%) and minor biotite (~5%) with accessory minerals of allanite, apatite, zircon and opaque oxide minerals (Figure 3c,d). K–feldspar and plagioclase have undergone varying degrees of sericitization. Biotites commonly occur as fragments and have been altered by some degree of chloritization. Some apatite crystals are distributed as assemblages within the biotitic fragments. Except for some big plagioclase crystals, minerals are almost fine-grained with equigranular texture, revealing that the BCD granites belong to hypabyssal intrusive rocks.

The BCN granites comprise sphene–biotite and sphene–hornblende–biotite granitic porphyries. The former consists of perthite (50%–55%), quartz (20%–25%), plagioclase (25%–35%) and minor biotite (<8%) with accessory minerals including sphene, allanite, apatite, zircon, rutile and opaque oxide minerals (Figure 3e). Perthite phenocryst shows Carlsbad twin and is partially altered to albite. Some plagioclases have experienced sericitization. Biotite is altered to muscovite and develops apatite aggregates internally. We observe that these plagioclase, quartz and biotite are deformed by force in the groundmass. The latter has similar petrographic characteristics to those of the former (Figure 3f). It is composed of perthite (50%–55%), quartz (20%–25%), plagioclase (25%–35%) and minor biotite (<5%) and hornblende (<2%) with accessory minerals including sphene, allanite, apatite, zircon and opaque oxide minerals. Perthite phenocryst exhibits less degrees of albitization than that of the former. Sericitization in plagioclase is obvious, and hornblende within the perthite phenocryst is altered locally to biotite. Biotite has been altered with varying degrees of chloritization. Plagioclase, quartz and biotite are deformed by force in the groundmass.

The TL granites are fine-grained allanite–biotite granite porphyries, and their mineral compositions consist of perthite (40%–55%), plagioclase (25%–35%), quartz (20%–30%) and minor biotite (~5%) with accessory minerals of allanite, apatite, zircon and opaque oxide minerals (Figure 3g,h). Perthite phenocryst exhibits Carlsbad twin, and plagioclase phenocrysts display polysynthetic twin with common sericitization. Force deformation can be observed for plagioclase, quartz and biotite, and some of them have been altered by the pelletization process (Figure 3g,h). Myrmekitic texture is developed among these crystals of perthite, plagioclase, quartz and biotite.

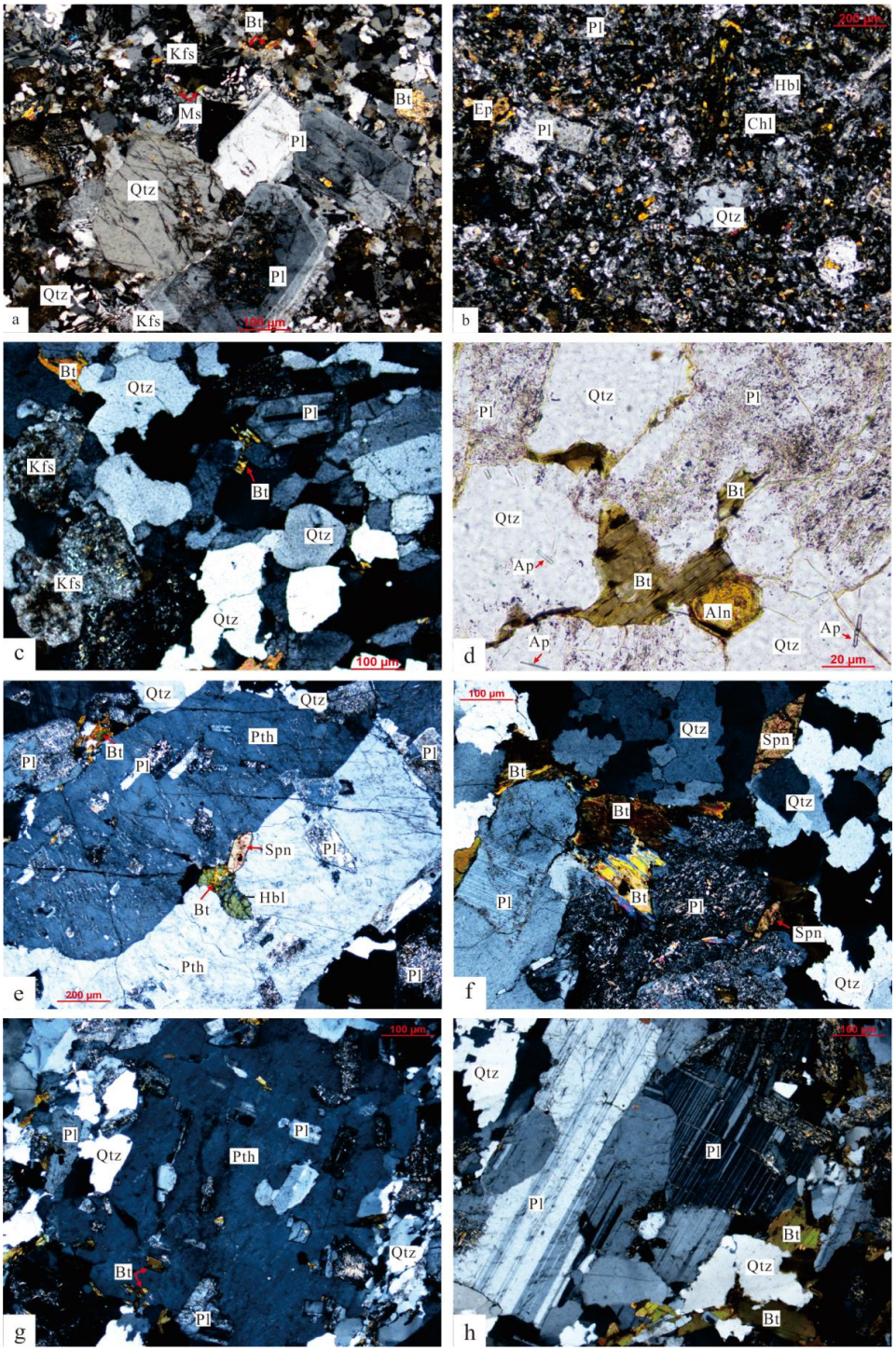

Figure 3. Representative photomicrographs of the Yilashan and Amdo granitoids in the Nagqu area. (**a**) Graphic–myrmekitic textures of granophyres (YLSS–2); (**b**) mineral compositions of quartz diorite–porphyrites (YLSZ–5); (**c**) granite containing K–feldspar, plagioclase, quartz and minor biotite (sample BCD–1); (**d**) biotites occurring as fragments (sample BCD–1); (**e**) Perthite showing Carlsbad twin and containing hornblende and sphene (sample BCN–2); (**f**) plagioclase, quartz and minor biotite and sphene association in granite (sample BCN–1); (**g**,**h**) mineral assemblage of the sample TL–1. The abbreviations for minerals: Qtz, quartz; Pl, plagioclase; Kfs, K–feldspar; Hbl, hornblende; Chl, Chlorite; Ep, epidote; Pth, perthite; Aln, allanite; Spn, sphene; Bt, biotite; Ap, apatite; Ms, muscovite.

4. Analytical Methods

4.1. Zircon U–Pb and In Situ Lu–Hf Isotopic Analyses

Zircons were obtained by conventional density and magnetic separation methods. After being handpicked under a binocular microscope, representative grains were mounted in epoxy resin and then polished down to expose their cores. Transmitted and reflected light and cathodoluminescence (CL) microscopy images were taken to characterize external morphology and internal structures and to choose optimum spots for U–Pb dating and in situ Lu–Hf isotopic analyses. Microscopy images were photographed at the Yujin Technology Co., Ltd., Chongqing, China.

Zircon U–Pb isotopic analyses were done on a Coherent GeoLasPro 193–nm laser ablation system in combination with an Agilent 7700x inductively coupled plasma mass spectrometer (LA–ICP–MS) at the Guangdong Provincial Key Laboratory of Marine Resources and Coastal Engineering (GPKLMRCE), Sun Yat–sen University, Guangzhou, China. Analyses of zircons were carried out using a spot diameter of 32 μm, a repetition rate of 5 Hz, and a constant energy of 41 mJ/cm^2. Each analysis incorporated a background acquisition of 20 s followed by a signal acquisition of 45 s. The 91,500 standard zircon was used as an external standard for U–Pb dating, and the NIST SRM 610 glass was adopted as an external standard to ensure machine optimization. Every five sample analyses were followed by analyses of standards. ^{29}Si was used as an internal standard for the calibration of U, Th and Pb concentrations. Zircon U–Pb raw data and trace elemental compositions were calculated offline using ICPMSDataCal [65]. Concordia diagram and weighted mean age calculation were performed using Isoplot/Ex version 3.0 [66]. Individual U–Pb analyses are quoted at the 1σ level. The detailed analytical methods are described in [65], and the analytical results are presented in Table S1.

In situ zircon Hf isotopic analyses of these samples were done using an ESI NWR193 laser ablation microprobe attached to a Neptune plus multi-collector inductively coupled plasma mass spectrometer (ICP–MS) at the CreaTech Testing International Co., Ltd., Beijing, China. Zircons were ablated with a spot diameter of 40 μm. The initial ^{176}Hf/^{177}Hf ratios were calculated based on the ^{176}Lu decay constant of 1.867 × 10 $^{-11}$ year $^{-1}$ presented by [67] and the measured ^{176}Hf/^{177}Hf values. The present-day chondritic ^{176}Lu/^{177}Hf (0.0332) and ^{176}Hf/^{177}Hf (0.282772) values reported by [68] were used for the calculation of ε_{Hf} (t) values. Single-stage model ages (T_{DM1}) were calculated according to the depleted mantle ^{176}Lu/^{177}Hf (0.0384) and ^{176}Hf/^{177}Hf (0.28325) ratios at present-day [69], and two-stage model Hf ages (T_{DM2}) were calculated based on an assumed average value of ^{176}Lu/^{177}Hf (0.015) for average continental crust [70]. During the data acquisition period, the GJ1 standard zircon was used to evaluate the reliability of the data. The weighted mean ^{176}Hf/^{177}Hf ratios of the GJ1 standard zircon (0.282014 ± 44 (2σ, *n* = 10) for YLSZ and YLSS samples; 0.281997 ± 26 (2σ, *n* = 10) for BCD, BCN and TL samples) resemble the value obtained by [71]. The detailed analytical methods are presented by [72,73]. The zircon in situ Lu–Hf isotopic data are listed in Table S2.

4.2. Whole-Rock Major and Trace Element Analyses

After the removal of altered surfaces, representative granitoids samples were crushed to powders of 200 mesh using a tungsten carbide ball mill before geochemical analyses.

The measurement of whole-rock major element compositions of all samples was carried out using a PANalytical Axios X–ray fluorescence (XRF) spectrometer at the ALS Chemex Co., Ltd., Guangzhou, China. During the measuring, the standard samples LAT–CS9, SARM–32, SARM–43, SARM–45 and NCSDC–73303 were used in different test batches for the validation of analytical accuracy. The general methods resemble those described by [74] and have analytical accuracies better than ± 1%–2%. For whole-rock trace element analyses, the samples YLSS–2, –3, –4, BCD–1, –2, –4, BCN–1, –2, –3, –6 and TL–1, –3, –4 were analyzed using a Perkin–Elmer Sciex ELAN 6000 ICP–MS at the State Key Laboratory of Ore Deposit Geochemistry, Institute of Geochemistry (Guiyang), Chinese Academy of Sciences. Standard samples, including OU–6, AMH–1 and GBPG–1, were

measured in different test batches to monitor analytical accuracy. The analytical accuracies are better than ±5%. Similarly, the determination of the whole-rock trace element data of remaining samples were carried out using a Perkin–Elmer Sciex ELAN 6000 ICP–MS at the ALS Chemex Co., Ltd., Guangzhou, China. Standard samples, including OGGeo–08, OREAS–45e, OREAS–120, OREAS–100a, GBW07104, GBW07105, GBW07108, NCSDC47009, SARM–4 and SARM–5 were adopted in different test batches to monitor analytical accuracy. The general analytical methods are similar to those presented by [74], and the analytical precisions for most elements are better than ±5%. Analytical data are presented in Table S3.

4.3. Whole-Rock Sr–Nd Isotopic Analyses

Whole-rock Sr–Nd isotopic analyses were carried out using a Finnigan MAT–261 thermal ionization mass spectrometer (TIMS) at the State Key Laboratory of Geological Processes and Mineral Resources (SKLGPMR), China University of Geosciences (Wuhan), China. Approximately 0.1 g of whole-rock powder was dissolved in Teflon beakers with a mixture of HF + HNO_3 acids, and Sr and Nd were subsequently separated and purified using standard ion exchange chemical techniques. Total procedural blanks are <200 pg for Sm and Nd, and <500 pg for Rb and Sr. The detailed analytical methods resemble those described in [75]. Measured $^{87}Sr/^{86}Sr$ and $^{143}Nd/^{144}Nd$ ratios were corrected for instrumental mass fractionation via normalizing to $^{86}Sr/^{88}Sr = 0.1194$ and $^{146}Nd/^{144}Nd = 0.7219$, respectively. The reported $^{87}Sr/^{86}Sr$ and $^{143}Nd/^{144}Nd$ ratios were adjusted to the NBS 987 standard of $^{87}Sr/^{86}Sr = 0.71025$ and the La Jolla Nd standard of $^{143}Nd/^{144}Nd = 0.511860$, respectively. Analytical results are listed in Table S3.

5. Results

5.1. Zircon U–Pb Ages and Lu–Hf Isotopic Compositions

Zircons collected from eight samples are euhedral to subhedral and stubby to elongated prismatic, and these grains range in length from 100 to 300 μm with length/width ratios of 1:1 to 3:1 (Figure S1). The core–rim structure is common, and most of the zircons exhibit well-developed oscillatory zoning with various luminescence signals in CL images that resemble that of magmatic zircons (Figure S1).

5.1.1. YLSZ–9 (Quartz Diorite–Porphyrite)

Twenty-four analyses on 24 spots were conducted on 23 zircons (including those from inner cores) (Figure S1a), which yield a broad range of U (119–3265 ppm) and Th (49–5404 ppm) concentrations with a wide range of Th/U ratios of 0.1–4.6 (Table S1). The younger age group having nine analyses yields $^{206}Pb/^{238}U$ ages of 104.7 ± 2.3 to 110.3 ± 2.4 Ma and a weighted mean $^{206}Pb/^{238}U$ age of 108.0 ± 1.5 Ma (MSWD = 0.53, $n = 9$; Figure 4a). This age represents the crystallization age of this sample. The initial $^{176}Hf/^{177}Hf$ ratios of this group range from 0.282421 to 0.282585, corresponding to the $\varepsilon_{Hf}(t)$ values ranging from –10 to –4.3 (Figure 5), and T_{DM2} ages from 1.44 to 1.80 Ga (Table S2). The older grains yield U–Pb ages ranging from 2510.2 to 175.6 Ma (five spots with $^{206}Pb/^{238}U$ ages > 1000 Ma do not show in Figure 4a; Table S1). Taking their CL features (Figure S1a), we infer that these ages define the crystallization ages of inherited or captured zircons from the source region. The $(^{176}Hf/^{177}Hf)_i$ ratios, $\varepsilon_{Hf}(t)$ values and T_{DM2} ages range from 0.281535 to 0.282367, –23.6 to +12.1 (Figure 5) and 1.36 to 2.92 Ga, respectively (Table S2).

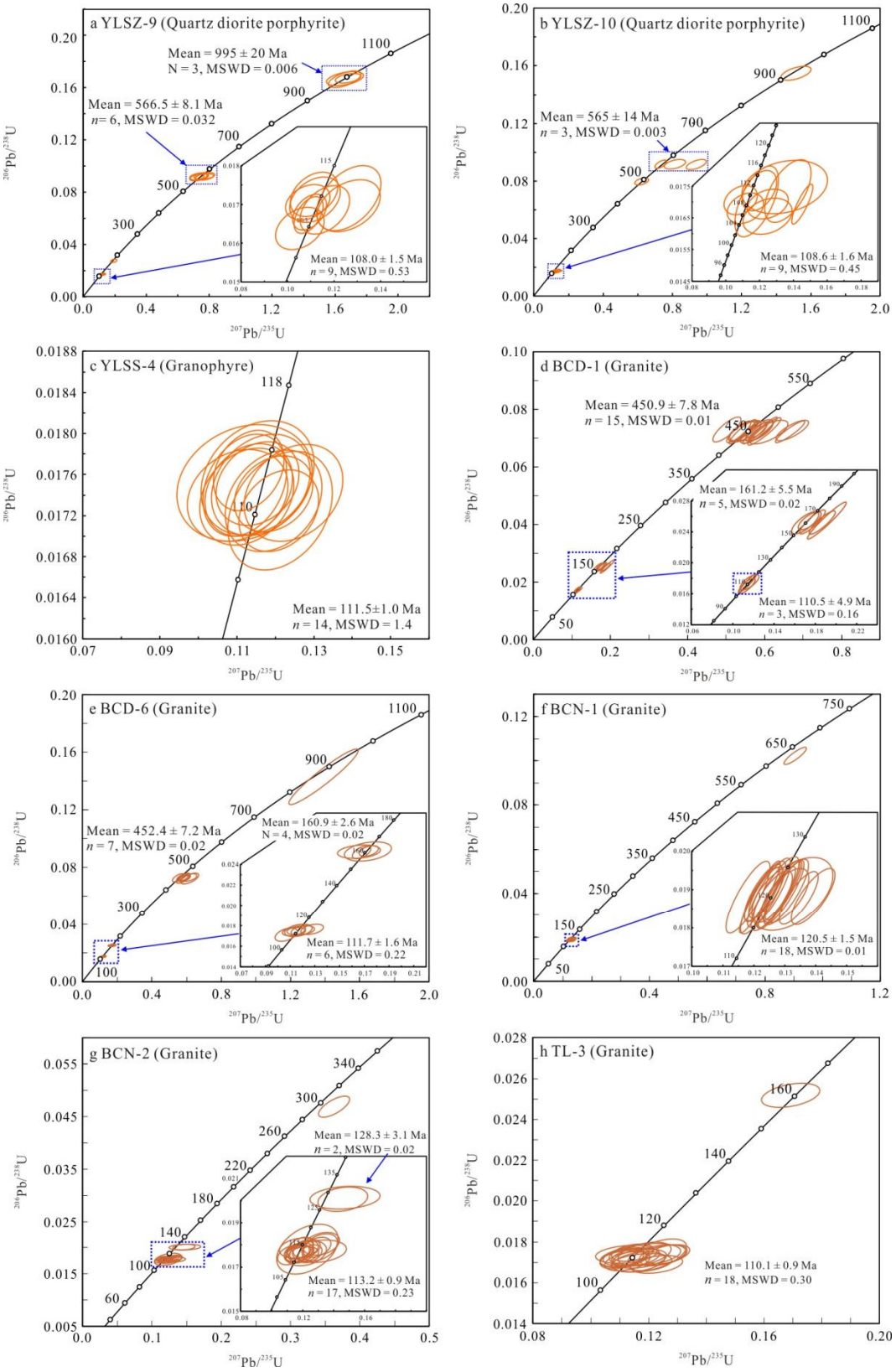

Figure 4. Zircon LA–ICP–MS U–Pb concordia (left) and probability density function (right) diagrams of the analyzed zircons from the Yilashan and Amdo granitoids in the Nagqu area. (**a**): YLSZ–9; (**b**): YLSZ–10; (**c**): YLSS–4; (**d**): BCD–1; (**e**): BCD–6; (**f**): BCN–1; (**g**): BCN–2; (**h**): TL–3.

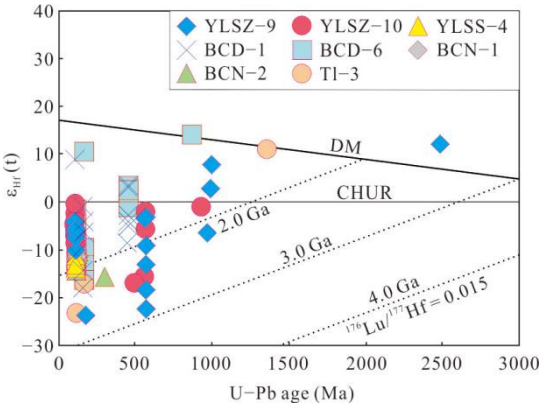

Figure 5. Zircon $\varepsilon_{Hf}(t)$ versus U–Pb age diagram for the Yilashan and Amdo granitoids in the Nagqu area. DM: depleted mantle; CHUR: chondritic uniform reservoir.

5.1.2. YLSZ–10 (Quartz Diorite–Porphyrite)

Twenty-two analyses on 22 spots were obtained from 22 zircons (Figure S1b) and yield a broad range of U (57–12806 ppm) and Th (18–6967 ppm) concentrations with Th/U ratios of 0.1–2.2 (Table S1). The younger age group has nine analyses and yields $^{206}Pb/^{238}U$ ages ranging from 105.8 ± 2.4 to 111.7 ± 3.5 Ma with a weighted mean $^{206}Pb/^{238}U$ age of 108.6 ± 1.6 Ma (MSWD = 0.45, n = 9; Figure 4b). This age defines the crystallization age of this sample. The $(^{176}Hf/^{177}Hf)_i$ ratios of this group range from 0.282451 to 0.282690, corresponding to the $\varepsilon_{Hf}(t)$ data ranging from −8.9 to −0.5 (Figure 5), and T_{DM2} ages from 1.20 to 1.73 Ga (Table S2). The older grains yield U–Pb ages ranging from 3417.0 to 493.8 Ma (Figure 4b; Table S1). In view of their CL features (Figure S1b), we infer that these ages represent the crystallization ages of inherited or captured zircons from the source region. The $(^{176}Hf/^{177}Hf)_i$ ratios, $\varepsilon_{Hf}(t)$ values and T_{DM2} ages range from 0.281973 to 0.282362, −17.1 to −1.3 (Figure 5) and 1.64 to 2.53 Ga, respectively (Table S2).

5.1.3. YLSS–4 (Granophyre)

Fourteen spot analyses were obtained from 14 zircon grains (Figure S1c). The U and Th concentrations are 192–516 ppm and 211–620 ppm, respectively, with Th/U ratios of 1.0–1.5 (Table S1). The data yield concordant $^{206}Pb/^{238}U$ ages ranging from 110.2 ± 2.4 to 112.7 ± 1.6 Ma, with a weighted mean age of 111.5 ± 1.0 Ma (MSWD = 0.14, n = 14; Figure 4c). This age defines the crystallization age of this sample. The initial $^{176}Hf/^{177}Hf$ ratios range from 0.282311 to 0.282392, corresponding to the $\varepsilon_{Hf}(t)$ values of –13.8 to –11.0 (Figure 5), and T_{DM2} ages of 1.86 to 2.04 Ga (Table S2).

5.1.4. BCD–1 (Granite)

Twenty–four analyses on 24 spots for this sample have varied U (66–2285 ppm) and Th (67–1300 ppm) contents, with Th/U ratios of 0.1–1.5 (Table S1). The younger age group consists of three spots that yields $^{206}Pb/^{238}U$ ages of 108.7 ± 4.1 to 111.9 ± 4.1 Ma and a weighted mean $^{206}Pb/^{238}U$ age of 110.5 ± 4.9 Ma (MSWD = 0.16, n = 3; Figure 4d). This age represents the crystallization age of this sample. The initial $^{176}Hf/^{177}Hf$ ratios of this group range from 0.282472 to 0.282774, corresponding to the ε_{Hf} values of −8.2 to 2.5 (Figure 5), and T_{DM2} ages of 1.01 to 1.68 Ga (Table S2). The older grains yield U–Pb ages ranging from 1255.6 to 160.4 Ma (Figure 4d; Table S1). Considering their CL features (Figure S1d), we infer that these ages define the crystallization ages of inherited or captured zircons from the source region. The $(^{176}Hf/^{177}Hf)_i$ ratios, $\varepsilon_{Hf}(t)$ values and T_{DM2} ages range from 0.282295 to 0.282588, –12.0 to –0.6 (Figure 5) and 1.39 to 1.97 Ga, respectively (Table S2).

5.1.5. BCD–6 (Granite)

Nineteen analyses on 19 spots for this sample show varied U (206–3105 ppm) and Th (86–3099 ppm) contents, with their Th/U ratios of 0.1–4.0 (Table S1). The younger age group

has six spots that yields concordant or nearly concordant $^{206}Pb/^{238}U$ ages of 109.3 ± 2.7 to 112.7 ± 2.1 Ma and a weighted mean $^{206}Pb/^{238}U$ age of 111.7 ± 1.6 Ma (MSWD = 0.22, *n* = 6; Figure 4e). This age represents the crystallization age of this sample. The initial $^{176}Hf/^{177}Hf$ ratios of this group range from 0.282453 to 0.282619, corresponding to the ε_{Hf} values varying from −8.8 to −3.0 (Figure 5), and T_{DM2} ages from 1.36 to 1.73 Ga (Table S2). The older grains yield U–Pb ages ranging from 1116.7 to 160.4 Ma (Figure 4e; Table S1). Considering their CL features (Figure S1e), we infer that these ages define the crystallization ages of inherited or captured zircons from the source region. The $(^{176}Hf/^{177}Hf)_i$ ratios, $\varepsilon_{Hf}(t)$ values and T_{DM2} ages range from 0.282364 to 0.282769, −10.9 to +5.4 (Figure 5) and 0.99 to 1.90 Ga, respectively (Table S2).

5.1.6. BCN–1 (Granite)

Nineteen analyses on 19 spots for this sample display varied U (445–2051 ppm) and Th (138–2535 ppm) contents, with Th/U ratios of 0.3–3.0 (Table S1). The younger age group contains eighteen spots that yields concordant or nearly concordant $^{206}Pb/^{238}U$ ages ranging from 120.0 ± 2.9 to 121.1 ± 3.2 Ma with a weighted mean age of 120.5 ± 1.5 Ma (MSWD = 0.01, *n* = 18; Figure 4f). This age represents the crystallization age of this sample. The initial $^{176}Hf/^{177}Hf$ ratios of this group are 0.282450–0.282522, corresponding to the ε_{Hf} values varying from −8.7 to −6.2 (Figure 5), and T_{DM2} ages from 1.57 to 1.73 Ga (Table S2). Spot #23 was conducted on inner core domain (Figure S1f) and yields an oldest $^{206}Pb/^{238}U$ age of 627.4 ± 15.2 Ma. This age may define the crystallization age of captured zircon (Figure 4f).

5.1.7. BCN–2 (Granite)

Twenty analyses on 20 spots for this sample produce varied U (452–1277 ppm) and Th (174–2778 ppm) contents, with their Th/U ratios of 0.2–3.7 (Table S1). The younger age group has seventeen analyses which are concordant or nearly concordant, yielding $^{206}Pb/^{238}U$ ages of 112.0 ± 1.8 to 115.3 ± 2.1 Ma with a weighted mean $^{206}Pb/^{238}U$ age of 113.2 ± 0.9 Ma (MSWD = 0.23, *n* = 17; Figure 4g). This age represents the crystallization age of this sample. The initial $^{176}Hf/^{177}Hf$ ratios of this group range from 0.282419 to 0.282510, corresponding to the ε_{Hf} values varying from −10.0 to −6.8 (Figure 5), and T_{DM2} ages from 1.60 to 1.80 Ga (Table S2). The older grains yield $^{206}Pb/^{238}U$ ages ranging from 295.5 ± 8.2 Ma to 128.1 ± 2.3 Ma (Figure 4g; Table S1). Considering their signatures (Figure S1g), we suggest that these ages define the crystallization ages of inherited or captured zircons from the source region. The $(^{176}Hf/^{177}Hf)_i$ ratios, $\varepsilon_{Hf}(t)$ values and T_{DM2} ages range from 0.282286 to 0.282483, −10.7 to −7.8 (Figure 5) and 1.65 to 1.98 Ga, respectively (Table S2).

5.1.8. TL–3 (Granite)

Twenty analyses on 20 spots for this sample yield varied U (420–1646 ppm) and Th (285–4051 ppm) contents, with Th/U ratios of 0.2–2.9 (Table S1). The dominant age group has eighteen analyses which are concordant or nearly concordant, yielding $^{206}Pb/^{238}U$ ages of 108.1 ± 1.8 to 111.7 ± 1.7 Ma with a weighted mean $^{206}Pb/^{238}U$ age of 110.1 ± 0.9 Ma (MSWD = 0.30, *n* = 18; Figure 4h). This age represents the crystallization age of this sample. The initial $^{176}Hf/^{177}Hf$ ratios of this group range from 0.282290 to 0.282538, corresponding to the ε_{Hf} values of −14.6 to −5.9 (Figure 5), and T_{DM2} ages of 1.54 to 2.09 Ga (Table S2). The remaining grains yield U–Pb ages ranging from 1353.7 to 160.3 Ma (Figure 4h; Table S1). In view of their CL features (Figure S1h), we infer that these ages define the crystallization ages of inherited or captured zircons from the source region. The $(^{176}Hf/^{177}Hf)_i$ ratios, $\varepsilon_{Hf}(t)$ values and T_{DM2} ages range from 0.282031 to 0.282353, –11.3 to +3.0 (Figure 5) and 1.90 to 1.92 Ga, respectively (Table S2).

5.2. Whole-Rock Geochemical Compositions

The YLSZ quartz diorite–porphyritic samples yield a relatively narrow range of LOI (loss on ignition) values ranging from 2.19 to 2.91 wt.%, higher than those of the YLSS and Amdo granite samples (0.55–0.98 wt.%) (Table S3). These values indicate that the YLSS and Amdo granites are fresher than the YLZS quartz diorite–porphyrites.

5.2.1. YLSZ Quartz Diorite–Porphyrite

The quartz diorite–porphyritic samples exhibit a narrow range of major element contents with SiO_2 ranging from 61.29 to 63.22 wt.%, Al_2O_3 from 15.46 to 16.06 wt.%, MgO from 3.06 to 3.66 wt.%, Fe_2O_3T from 4.64 to 5.28 wt.%, TiO_2 from 0.49 to 0.53 wt.%, CaO from 2.94 to 4.61 wt.%, K_2O from 2.65 to 2.94 wt.% and Na_2O from 3.32 to 4.09 wt.% (Table S3). Their total alkali ($Na_2O + K_2O$) contents and Na_2O/K_2O ratios are 5.97–6.77 wt.% and 1.19–1.53, respectively. $Mg^{\#}$ values ($Mg^{\#} = 100 \times MgO/(MgO + FeO_T)$) range from 59.9 to 64.1. The samples feature high Al, Mg, Fe and total alkali contents. On the Harker diagram (Figure S2), the samples show nearly negative correlations of MgO, Al_2O_3, Fe_2O_{3T}, CaO, TiO_2, P_2O_5, Zr, Ni and V with SiO_2. They almost plot in the sub-alkaline diorite field on the total alkali–silica (TAS) diagram (Figure 6a) and belong to high-K calc-alkaline series on the SiO_2 versus K_2O diagram (Figure 6b). In addition, the quartz diorite–porphyrites yield high A/NK (molar $Al_2O_3/(Na_2O + K_2O)$; 1.64–1.89), but low A/CNK (molar $Al_2O_3/(CaO + Na_2O + K_2O)$; 0.94–1.06) ratios that they are metaluminous to weakly peraluminous on the A/CNK versus A/NK diagram (Figure 6c).

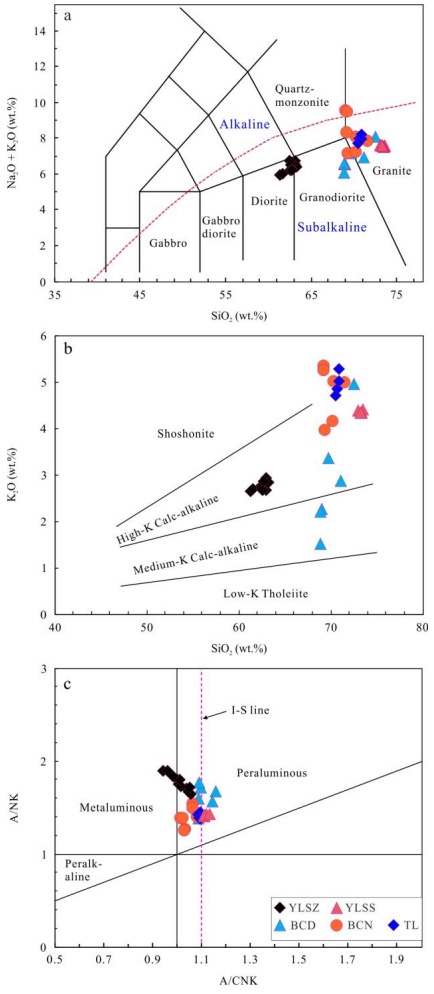

Figure 6. ($Na_2O + K_2O$) versus SiO_2 (**a**) [76]; K_2O versus SiO_2 (**b**) [77]; and A/NK versus A/CNK (**c**) [78] diagrams for the Yilashan and Amdo granitoids in the Nagqu area.

The total rare earth element (ΣREE) concentrations of the quartz diorite–porphyritic samples range from 131.9 to 145.94 ppm, with the average mean of 140.2 ppm (Table S3). $(La/Yb)_N$ (subscript "N" denotes normalization to chondrite values) ratios = 15.40–17.64, $(La/Sm)_N$ = 5.28–5.76, and $(Gd/Yb)_N$ = 1.84–2.00. The chondrite-normalized REE patterns of the quartz diorite–porphyrites exhibit significant LREE (light REE) enrichments with slight right dipping HREE (heavy REE) distributions (Figure 7a). They show weak negative Eu anomalies (Figure 7a) with δEu values of 0.71–0.92. On the primitive mantle-normalized multi-element spidergrams (Figure 7b), the quartz diorite–porphyrites are selectively enriched in large ion lithophile elements (LILEs; e.g., Rb and U), Th, Zr and Hf, but depleted in Ba and high-field strength elements (HFSEs; e.g., Nb, Ta and Ti) to varying degrees.

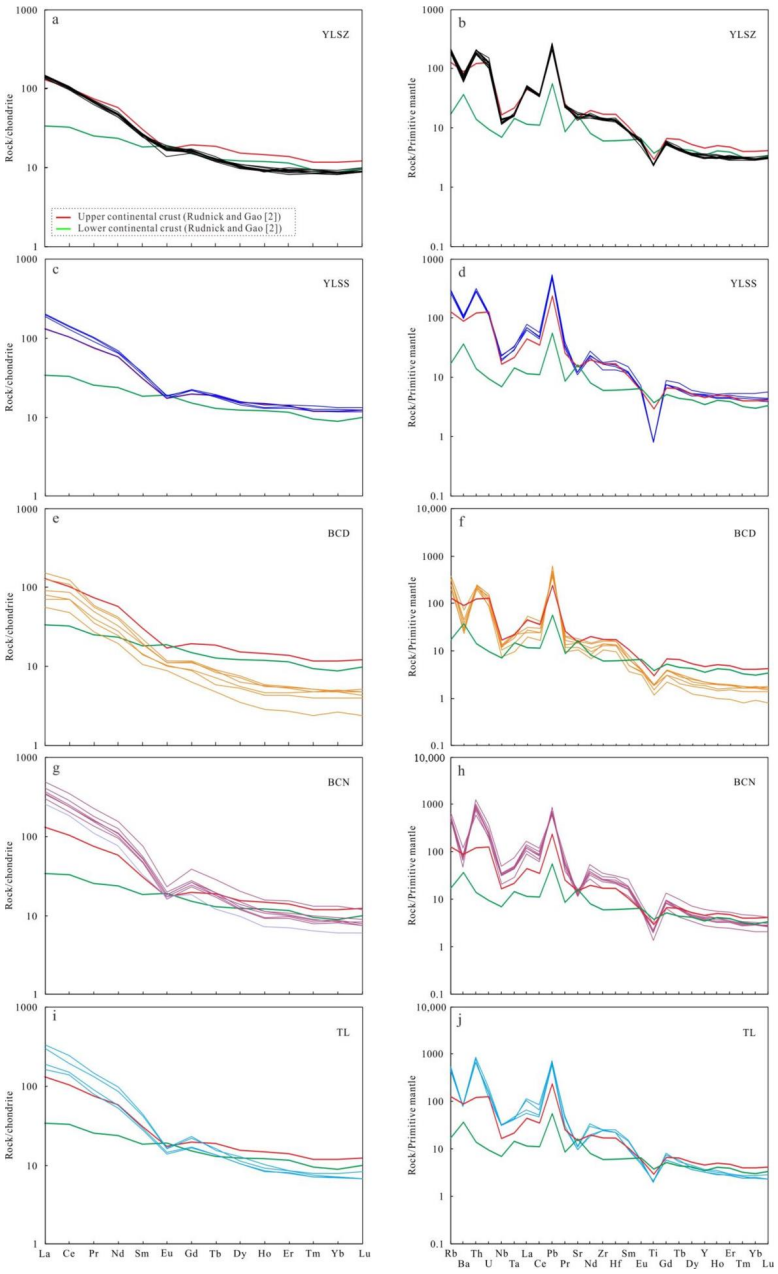

Figure 7. Chondrite-normalized REE (left) and primitive mantle-normalized trace element (right) patterns for the Yilashan and Amdo granitoids in the Nagqu area. The chondrite and primitive mantle normalization data are from [79]. Data for Upper and Lower continental crust are from [2]. (**a**):YLSZ; (**b**):YLSZ; (**c**): YLSS; (**d**): YLSS; (**e**):BCD; (**f**):BCD; (**g**): BCN; (**h**): BCN; (**i**): TL; (**j**): TL.

5.2.2. YLSS Granophyre

The granophyric samples have a narrow range of SiO_2 (73.0 wt.%–73.5 wt.%), Al_2O_3 (14.10 wt.%–14.40 wt.%), MgO (0.30 wt.%–0.34 wt.%), Fe_2O_{3T} (1.34 wt.%–2.00 wt.%), TiO_2 (0.17 wt.%–0.18 wt.%), CaO (1.45 wt.%–1.50 wt.%), K_2O (4.34 wt.%–4.40 wt.%) and Na_2O (3.21 wt.%–3.28 wt.%) contents (Table S3), with total alkali ($Na_2O + K_2O$) and Na_2O/K_2O values of 7.55 wt.%–7.64 wt.% and 0.73–0.76, respectively. $Mg^{\#}$ values range from 27.2 to 34.3. They contain higher SiO_2, K_2O and total alkali contents, but lower Al_2O_3, MgO, Fe_2O_{3T}, TiO_2 and CaO contents compared to those of the quartz diorite–porphyritic samples. On the Harker diagram (Figure S2), the granophyres roughly exhibit negative correlations of MgO, Al_2O_3, TiO_2, Zr and Ni with SiO_2, whereas show near constant values of CaO and V with SiO_2. Note that a positive correlation of Fe_2O_3T with SiO_2 (Figure S2c) may be due to the small number of granophyric samples analyzed in this paper. These samples plot in the sub-alkaline granite field on the TAS diagram (Figure 6a) and show high-K calc-alkaline features on the SiO_2 versus K_2O diagram (Figure 6b). In addition, they have high A/NK (1.41–1.43) and A/CNK (1.11–1.13) ratios that are strongly peraluminous on the A/CNK versus A/NK diagram (Figure 6c).

The granophyric samples exhibit their ΣREE concentrations ranging from 180.7 to 229.0 ppm, with the average value of 199.8 ppm (Table S3). $(La/Yb)_N$ ratios = 14.73–17.32, $(La/Sm)_N$ = 5.22–5.69, and $(Gd/Yb)_N$ = 1.67–1.86. The chondrite-normalized REE patterns of these samples are marked by apparent LREE enrichments with slight right dipping HREE distributions (Figure 7c). They feature strong negative Eu anomalies (Figure 7c) with δEu values being 0.63–0.67. On the primitive mantle-normalized multi-element spidergrams (Figure 7d), the granophyres are selectively enriched in LILEs (e.g., Rb and U), Th, Zr and Hf, but depleted in Ba, Sr and HFSEs (e.g., Nb, Ta and Ti) to varying degrees. They show more significant depletion in Eu, Sr and Ti compared to the quartz diorite–porphyritic samples (Figure 7a–d).

5.2.3. Amdo Granite

The BCD, BCN and TL granitic samples exhibit variable contents of SiO_2 (68.90 wt.%–72.5 wt.%), Al_2O_3 (13.85 wt.%–16.30 wt.%), K_2O (1.52 wt.%–5.33 wt.%) and Na_2O (2.80 wt.%–4.55 wt.%) (Table S3), with total alkali ($Na_2O + K_2O$) and Na_2O/K_2O values of 6.07 wt.%–8.27 wt.% and 0.55–2.99, respectively. They have relatively low MgO (0.54 wt.%–1.11 wt.%), Fe_2O_{3T} (2.00 wt.%–4.14 wt.%), TiO_2 (0.25 wt.%–0.66 wt.%) and CaO (1.44 wt.%–3.11 wt.%) contents, with $Mg^{\#}$ numbers of 30–44 (Table S3). Harker diagrams of MgO, Al_2O_3, Fe_2O_3T, TiO_2, P_2O_5, CaO, Ni, Zr and V versus SiO_2 for these rocks are shown in Figure S2 that most of them exhibit clear linear patterns. On the TAS diagram (Figure 6a), these samples mainly plot in the sub-alkaline granite field with some in the granodiorite zone. The BCD samples show wide K_2O contents that display medium- to high-K calc-alkaline characteristics on the SiO_2 versus K_2O diagram (Figure 6b). The BCN and TL samples have relatively high K_2O contents that straddle the boundary between the high-K calc-alkaline and shoshonite fields (Figure 6b). In addition, all the samples are weakly to strongly peraluminous (Figure 6c) with A/NK of 1.37–1.76 and A/CNK of 1.02–1.16.

The ΣREE concentrations of the granite samples are variable ranging from 60 to 457 ppm (Table S3). $(La/Yb)_N$ ratios = 14.70–42.80, $(La/Sm)_N$ = 4.87–7.62 and $(Gd/Yb)_N$ = 1.87–3.17. The chondrite-normalized REE patterns are marked by obvious LREE enrichments, slight right dipping HREE patterns and weak to obvious negative Eu anomalies (δEu = 0.43–0.93, excluding BCD–4 of 1.08; Figure 7e,g,i). Moreover, the samples are selectively enriched in LILEs (e.g., Rb and U), Th, Zr and Hf, but depleted in Ba, Sr, Nb, Ta, and Ti on the primitive mantle-normalized multi-element spidergrams (Figure 7f,h,j). The samples from the BCN and TL plutons show higher ΣREE concentrations, more obvious depletion in Eu and enrichment in Th and HFSEs (e.g., Nb, Ta, Zr and Hf) that are different from those of the BCD samples (Figure 7e–j), implying that they have different origins.

5.3. Whole-Rock Sr–Nd Isotopic Compositions

Initial Sr–Nd isotopic and $\varepsilon_{Nd}(t)$ values and Nd model ages (T_{DM}) of samples were calculated using their crystallization ages (Table S1). The $(^{87}Sr/^{86}Sr)_i$ and $(^{143}Nd/^{144}Nd)_i$ ratios of the YLSZ quartz diorite–porphyrites are 0.710606–0.710761 and 0.512030–0.512037, respectively, with the ε_{Nd} (t = 108 Ma) values ranging from –9.1 to –9.0 and T_{DM} ages ranging from 1.52 to 1.55 Ga (Table S3). The YLSS granophyres have the $(^{87}Sr/^{86}Sr)_i$ and $(^{143}Nd/^{144}Nd)_i$ ratios of 0.712085–0.712316 and 0.511872–0.511892, respectively, with their $\varepsilon_{Nd}(t)$ (t = 112 Ma) values of −12.1 to −11.7 and T_{DM} ages of 1.65–1.74 Ga (Table S3). The $(^{87}Sr/^{86}Sr)_i$ and $(^{143}Nd/^{144}Nd)_i$ values of the BCD granites are 0.710155–0.717792 and 0.511920–0.512086, respectively, with the ε_{Nd} (t = 111 Ma) values varying from −11.23 to −7.97 and T_{DM} ages from 1.29 to 1.74 Ga. The $(^{87}Sr/^{86}Sr)_i$ and $(^{143}Nd/^{144}Nd)_i$ ratios of the BCN granites range from 0.713413 to 0.714058 and 0.511925 to 0.511933, respectively. The $\varepsilon_{Nd}(t)$ (BCN–1, t = 121 Ma; BCN–4, t = 113 Ma) values range from –10.92 to –10.88, with T_{DM} ages of 1.38–1.48 Ga. The $(^{87}Sr/^{86}Sr)_i$ and $(^{143}Nd/^{144}Nd)_i$ data of the TL granites are 0.714097–0.714461 and 0.511917–0.511929, respectively, with the ε_{Nd} (t = 111 Ma) values between –11.31 and –11.08 and T_{DM} ages of 1.40–1.63 Ga. On the $(^{87}Sr/^{86}Sr)_i$–$\varepsilon_{Nd}(t)$ diagram (Figure 8), these samples almost plot near the end member of the lower crust of northern Tibet [80], but plot far away from the area of the Amdo orthogneiss [36].

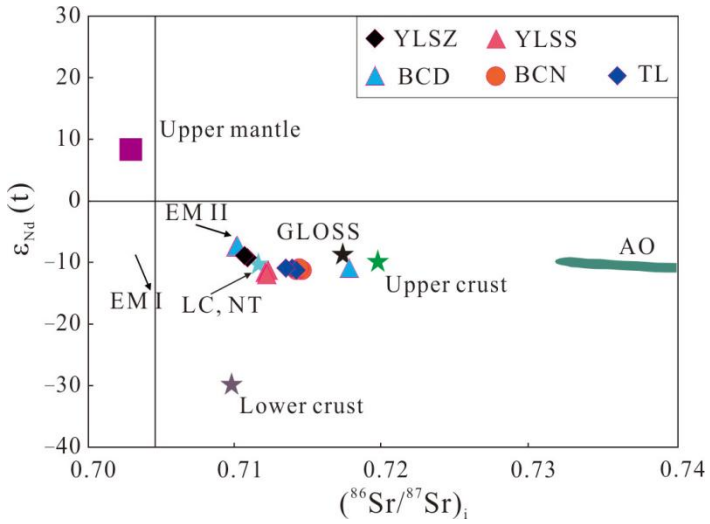

Figure 8. $(^{87}Sr/^{86}Sr)_i$ versus $\varepsilon_{Nd}(t)$ diagram for the Yilashan and Amdo granitoids in the Nagqu area. Upper mantle and upper crust data are from [81], and lower crust data are from [82]. Data for global subducting sediments (GLOSS), Amdo orthogneiss (AO) and lower crust of northern Tibet are from [36,80,83], respectively. EM: enriched mantle. Symbols as in Figure 6.

6. Discussion

6.1. Zircon U–Pb Ages and Implications

Early Cretaceous (140–100 Ma) intermediate-felsic igneous rocks occur widely in the northern Lhasa and Amdo terranes, which were likely formed related to the subduction and closure of the BNTO [7–9,11,18,56,84,85]. Our eight new crystallization ages of 121–108 Ma (Figure 4) are consistent with those of the Early Cretaceous magmatic rocks in the northern Lhasa and Amdo terranes.

The formation ages of the YLSS granophyres (~111.5 Ma) and the YLSZ quartz diorite–porphyrites (~108.0 and 108.6 Ma) are less than those of the Yilashan ophiolite (~184–133 Ma) [43,45,46], consistent with them occurring as dikes within the ophiolite. These ages, together with the collision related setting of the granophyres and quartz diorite–porphyrites defined in the following, suggest that the Yilashan ophiolite was formed prior to ~112 Ma at least.

As mentioned above, many inherited or captured zircons with variable U–Pb ages (~3417.0–1057.4 Ma, ~995.8–861.5 Ma, ~627.4 Ma, ~569.8–448.1 Ma, ~295.5 Ma, ~175.6–160.3 Ma and ~128.5–128.1 Ma) were obtained from the eight granitoid samples (Table S1). These ages reveal that the samples were produced with diverse magmatic sources and there was Precambrian crustal materials in the magma source that shows crustal reworking. The zircons from the YLSZ quartz diorite–porphyrites and the BCD granites yield U–Pb ages of ~995.8–861.5 Ma and ~569.8–448.1 Ma that agree with those of the Amdo orthogneisses (yielding crystallization ages of 920–820 Ma and 550–420 Ma [37]) in the Amdo terrane. In view of that, these rocks were likely developed in a collision related setting (see Section 6.3); the samplings of the quartz diorite–porphyrites are adjacent to the Amdo terrane (Figure 1c) and the corresponding magmatic CL-like zircons (Figure S1a,b,d,e), and these signatures suggest that the materials derived from the Amdo orthogneisses may be involved in the formation of the YLSZ quartz diorite–porphyrites and the BCD granites. However, these rocks plot far away from the Amdo orthogneiss field in Figure 8, implying that the addition of the Amdo orthogneisses in the generation of these rocks may be limited. Moreover, there are no zircons yielding U–Pb ages of ~920–820 Ma and ~550–420 Ma in the YLSS granophyres and the BCN and TL granites (Figure S1c,f,g,h). Combined with the different Sr–Nd isotopes from those of the Amdo orthogneisses (Figure 8), these signatures indicate the possibly absence or negligible addition of the Amdo orthogneisses in the formation of these rocks. In addition, the sample BCN–2 yields zircon U–Pb ages of ~128.5–128.1 and $\varepsilon_{Hf}(t)$ values of −7.4 to −7.8, agreeing with those of the Early Cretaceous granitoids (~140–100 Ma, –16.1 to +0.6, respectively) in the Amdo terrane [8,11,12,42]. Together with that, the zircons show magmatic CL-like signatures (Figure S1g) and yield high Th/U ratios (2.5–3.3; Table S1); these features may argue for the input of components derived from the Amdo Early Cretaceous (~140–100 Ma) granitoids in the formation of the BCN granites. Similarly, the sample YLSZ–9 yields a U–Pb age of ~175.6 Ma (Figure 3a) resembling that of the Yilashan ophiolite (~184–170 Ma [43,45]) and the metamorphosed ages (~190–169 Ma) of the Amdo orthogneisses [37,38]. However, considering the corresponding zircon yielding $\varepsilon_{Hf}(t)$ data of –23.6 and T_{DM2} age of 2.70 Ga (Table S2) and showing magmatic CL-like feature (Figure S1a) with Th/U ratio of 0.2, this grain with the U–Pb age of ~176 Ma was probably not derived from the Yilashan ophiolite and the Amdo orthogneisses.

Based on zircon Hf isotopic compositions of the Mesozoic–early Tertiary magmatic rocks occurred in the Amdo terrane, some workers argued that a Precambrian "hidden" crust was probably developed beneath the Amdo terrane [8,11]. A large area of Precambrian magma source existed beneath the central and eastern northern Lhasa and Amdo terranes [54]. In this paper, the zircon U–Pb ages of granitoid samples (Table S1), together with their $\varepsilon_{Hf}(t)$ values and T_{DM2} ages (Table S2) and the corresponding $\varepsilon_{Nd}(t)$ values and T_{DM} ages (Table S3), further suggest the presence of a Precambrian "hidden" crust beneath the northern Lhasa and Amdo blocks and it had played an important role in the magmatism of these areas.

6.2. Petrogenesis

6.2.1. YLSZ Quartz Diorite–Porphyrite

The quartz diorite–porphyritic samples yield low Nd/Th (1.16–1.56) and Nb/Ta (11.51–15.30) ratios, which are closer to those of crust (~3 and ~12, respectively [86]), but much lower than those of mantle-derived rocks (>15 and ~22, respectively [86]). Again, Ti/Zr values of the samples range from 19.12 to 21.04 that fall into the scope of continental crust rocks (<30 [87]). In addition, Rb/Sr ratios of these rocks are 0.33–0.42 that the average value of 0.38 is similar to that of crust (0.35 [88]). Together with the negative $\varepsilon_{Nd}(t)$ (−9.1 to −9.0) and zircon $\varepsilon_{Hf}(t)$ (−10.0 to −0.5) values with old Nd T_{DM} (1.52–1.55 Ga) and zircon Hf T_{DM2} (1.20–1.80 Ga) ages (Tables S2 and S3), these evidences indicate that the quartz diorite–porphyrites were probably mainly derived from a Paleo–Mesoproterozoic crustal source. Their inherited or captured zircons yielding older $^{207}Pb/^{235}U$ ages of 1002.0–3427.2 Ma

(Table S1) support this inference. Meanwhile, as discussed in Section 6.1, a small amount of components derived the Amdo orthogneisses may be involved in the formation of the quartz diorite–porphyrites. In addition, the quartz diorite–porphyrites yield a broad range of zircon $\varepsilon_{Hf}(t)$ values of −10.0 to −0.5 (Figure 5) and high MgO (3.06 wt.%–3.66 wt.%), $Mg^{\#}$ (59.9–64.1), Cr (97–110 ppm) and Ni (36.1–77.2 ppm) values (Table S3), suggesting a likely crust–mantle mixing origin. However, their relatively high SiO_2 (61.29 wt.%–63.22 wt.%) and Al_2O_3 (15.46–16.06 wt.%) contents and the overall high negative $\varepsilon_{Nd}(t)$ and zircon $\varepsilon_{Hf}(t)$ values (Figures 5 and 8) argue for an insignificant input of mantle-derived melts.

Experimental petrology shows that quartz diorites can be produced by partial melting of metapelite, metagraywacke, and metabasaltic to metatonalitic rocks [89–93]. CaO/Na_2O ratios are often used to determine the compositions of magma source of granitoids. CaO/Na_2O ratios < 0.5 indicate pelite-derived magmas, and those between 0.3–1.5 support melts derived from graywacke or igneous sources [94]. In this paper, the quartz diorite–porphyritic samples have high CaO/Na_2O ratios of 0.72–1.39 with the average value of 1.02, showing that they may be formed by partial melting of graywackes or igneous rock sources. Discrimination diagrams based on whole-rock major elements can be used to assess magma sources. In the diagram of ($CaO + MgO + FeO_T + TiO_2$) versus $CaO/(MgO + FeO_T + TiO_2)$ (Figure 9a), the quartz diorite–porphyritic samples exhibit low $CaO/(MgO + FeO_T + TiO_2)$ but high ($CaO + MgO + FeO_T + TiO_2$) contents that fall into the partial melts from the amphibolite field. This conclusion can also be drawn from the ($Al_2O_3 + MgO + FeO_T + TiO_2$) versus $Al_2O_3/(MgO + FeO_T + TiO_2)$ diagram (Figure 9b). In fact, experimental studies suggest that dehydration melting of amphibolite can produce melts of felsic to intermediate calc-alkaline compositions (e.g., diorite) [89,91]. Thus, the quartz diorite–porphyritic samples were probably derived from the partial melting of an amphibolitic/or metabasaltic magma source [95].

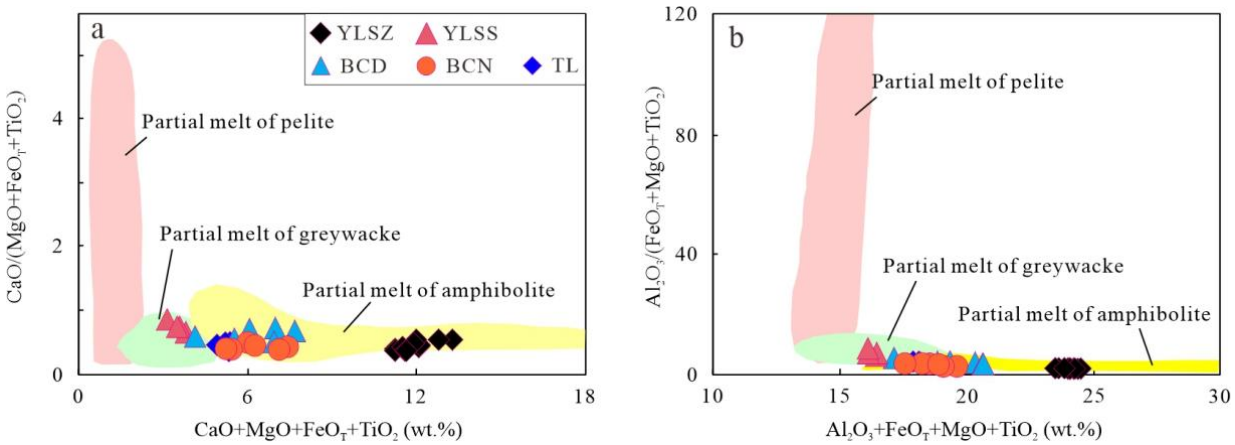

Figure 9. ($CaO + MgO + FeO_T + TiO_2$) versus $CaO/(MgO + FeO_T + TiO_2$) (**a**) and ($Al_2O_3 + MgO + FeO_T + TiO_2$) versus $Al_2O_3/(MgO + FeO_T + TiO_2$) (**b**) diagrams [96] for the Yilashan and Amdo granitoids in the Nagqu area. Symbols as in Figure 6. Fields are from [97–100].

In Figure S2, the YLSZ quartz diorite–porphyrites generally show negative correlations of MgO, Al_2O_3, Fe_2O_{3T}, TiO_2, P_2O_5, CaO, Ni, Zr and V with SiO_2. These correlations, together with the depletions in Eu, Sr and Ti in Figure 7a,b, imply the removal of plagioclase, K–feldspar, hornblende, Fe–Ti oxides, zircon and apatite during the magma evolution. In addition, Al_2O_3 content in quartz dioritic magma is diagnostic for pressure [101]. According to the partial melting experiments of amphibolite/eclogite, melts having Al_2O_3 contents lower than 15 wt.% indicate very low degrees of partial melting (≤5%–10%) at a pressure of ≤16 kbar, and the residual assemblage contains amphibole and plagioclase; whereas those >15.5 wt.% reflect moderate degrees of partial melting (10%–40%) when the pressure is >16 kbar, with the residual clinopyroxene, garnet and plagioclase [101]. The YLSZ quartz diorite–porphyrites, which yield Al_2O_3 contents of 15.46 wt.%–16.06 wt.% with the average

value of 15.75 higher than 15.5 wt.%, are indicative that they were possibly produced at >16 kbar with a moderate degree of partial melting and the residual assemblages have garnet, clinopyroxene and plagioclase. The residual garnet and plagioclase agree with these rocks yielding low Lu/Tb ratios (0.44–0.52), apparent LREE enrichments with depleted HREE patterns and observed depletions of Eu and Sr (Figure 7a,b).

6.2.2. YLSS Granophyre

Chemical composition is the most objective of all the possible classification criteria for granite types as granites are generally subdivided into I-, A-, S- and M-types based on their different geochemical compositions [102–104]. The granophyric samples exhibit high SiO_2 (73.0 wt.%–73.5 wt.%) and K_2O (4.34 wt.%–4.40 wt.%) contents (Table S3) that exclude their M-type affinity [102]. More evidences for this conclusion are given by their high $(^{87}Sr/^{86}Sr)_i$ (0.712187 to 0.712316) and low $\varepsilon_{Nd}(t)$ (−12.1 to −11.7) and zircon $\varepsilon_{Hf}(t)$ (−13.8 to −11.0) values (Tables S2 and S3), which are inconsistent with those of M-type granites [105]. The granophyres plot in the fractionated and unfractionated granite fields on the 10,000 × Ga/Al versus (Zr + Nb + Ce + Y) diagram (Figure 10a) and fall into the I-, S- and M-type zone on the 10,000 × Ga/Al versus Zr diagram (Figure 10b), suggesting that they may be I- or S-type granites. Generally, I-type granites are metaluminous to weakly peraluminous (A/CNK < 1.1), and S-type granites are obviously peraluminous (A/CNK > 1.1). The granophyric samples have: (1) obviously peraluminous features with A/CNK > 1.1 (Figure 6c); (2) a positive correction between SiO_2 and P_2O_5 (Figure S2f); (3) high K_2O/Na_2O ratios of 1.32–1.37; (4) high SiO_2 contents of 73.0–73.5 wt.% (Table S3); (5) strongly peraluminous minerals, such as muscovite, with the absence of hornblende (Figure 2a); and (6) relatively low zircon saturation temperatures of 787–815 °C with a mean of 805 °C (Table S3). These signatures suggest that the YLSS granophyres likely belong to S-type granites.

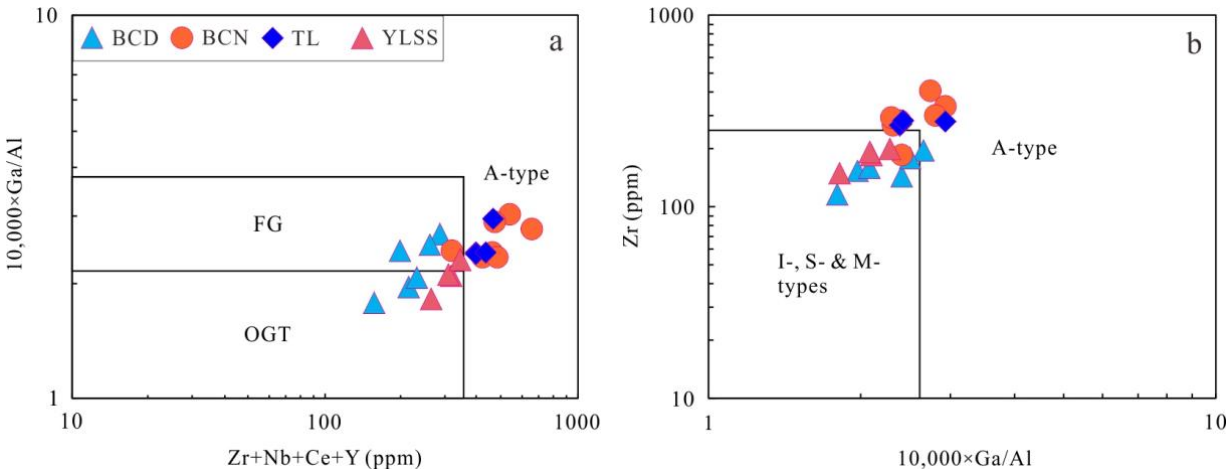

Figure 10. Plots of 10,000 × Ga/Al versus (Zr + Nb + Ce + Y) (**a**) and Zr (**b**) [98] for the Yilashan and Amdo granitoids in the Nagqu area. Symbols as in Figure 6. FG: fractionated felsic granites; OGT: unfractionated M-, I- and S-type granites.

Geochemical compositions of granite are affected by several factors that include the compositions of magma sources, partial melting, fractional crystallization, magma mixing and country-rock assimilation [106–109]. The granophyric samples have low Nd/Th (1.23–1.42), Nb/Ta (11.33–12.46) and Ti/Zr (5.15–6.88) ratios resembling those of crust [86,87], indicating that these rocks were likely derived from a crustal source. Again, they yield a narrow range of zircon $\varepsilon_{Hf}(t)$ values ranging from –13.8 to –11.0 (Figure 5) with T_{DM2} ages of 1.86–2.04 Ga (Table S2). Combined with their narrow range of $\varepsilon_{Nd}(t)$ values (–12.1 to –11.7) and Nd T_{DM} ages (1.65–1.74 Ga) (Table S3), these evidences indicate that the granophyric samples were probably derived from Paleoproterozoic crust. As discussed

above, the granophyric samples feature peraluminous and S-type granitic affinities. Previous studies shown that peraluminous granites can be derived from continental crustal sources involving metapelite, graywacke and metaigneous rocks [3,97,110–112]. The granophyric samples have relatively low MgO (0.30 wt.%–0.34 wt.%), Fe_2O_{3T} (1.34 wt.%–2.00 wt.%) and TiO_2 (0.17 wt.%–0.18 wt.%) contents; thus suggesting that metaigneous rocks are unlikely to be their magma sources. In Figure 9a, the granophyric samples display low (CaO + MgO + FeO_T + TiO_2) and CaO/(MgO + FeO_T + TiO_2) values that fall into the graywacke field, implying that they may be derived from the partial melting of a graywacke source. This inference is further confirmed by their low Al_2O_3/(MgO + FeO_T + TiO_2) and (Al_2O_3 + MgO + FeO_T + TiO_2) values (Figure 9b) and is also consistent with the conclusion that S-type granites originate from sedimentary rocks [113]. Moreover, an obvious contribution of juvenile components would apparently change the peraluminous affinities of magmas [114,115]. High-silica S-type granites yielding SiO_2 contents higher than 70 wt.% likely represent pure crustal melts [3]. The granophyric samples are peraluminous (Figure 6c) and exhibit high SiO_2 (73.0 wt.%–73.5 wt.%), but low MgO (0.30 wt.%–0.34 wt.%), Cr (8.25–13.2 ppm) and Ni (6.4–14.5 ppm) contents (Table S3); thus revealing no contribution of mantle-derived melts in their petrogenesis.

The YLSS granophyres exhibit roughly negative correlations of MgO, Al_2O_3, TiO_2, Ni and Zr with SiO_2 in Figure S2. These features, along with the variable depletions in Eu, Sr and Ti in Figure 6c,d, reflect the removal of plagioclase, K–feldspar, biotite, hornblende, Fe–Ti oxides and zircon during the evolution of magmas. In addition, garnets are mainly enriched in HREEs. The granophyric samples shows strongly fractionated REE patterns (Figure 7c) with high $(La/Yb)_N$ (14.73–17.32) and $(Dy/Yb)_N$ (1.13–1.20) ratios, indicating residual garnets in the source regions during crustal melting. These samples yield the average $(Dy/Yb)_N$ ratio of 1.18 that is lower than that of the YLSZ quartz diorite–porphyrites (1.20), suggesting that the latter may be derived from a relatively deeper source with more residual garnets.

6.2.3. BCD, BCN and TL Granites

The BCD, BCN and TL granitic samples have variable K_2O contents of 1.52 wt.%–5.33 wt.% and do not expose in ophiolite. Again, they yield high $(^{87}Sr/^{86}Sr)_i$ (0.710155–0.717792) and low $\varepsilon_{Nd}(t)$ (–11.31 to –7.97) and zircon $\varepsilon_{Hf}(t)$ (–15.6 to +5.4) values (Tables S2 and S3). Thus, the BCN, BCD and TL granites do not belong to M-type granites.

The BCD granites plot in the fields of fractionated and unfractionated granites on the 10,000 × Ga/Al versus (Zr + Nb + Ce + Y) diagram (Figure 10a), and basically fall into the I-, S- and M-type field on the 10,000 × Ga/Al versus Zr diagram (Figure 10b). Again, these samples show medium- to high-K calc-alkaline and roughly weakly peraluminous affinities (Figure 6b,c) and contain biotite, allanite, sphene with the absence of pyroxene and fayalite (Figure 3c,d) that are consistent with the features of I-type granites. Note that some I-type granites also exhibit strongly peraluminous signatures with A/CNK > 1.1 and are generally charactered by low K_2O/Na_2O ratios (<1.0) [110,116,117]. The samples BCD–3 and –5 yield high A/CNK values of 1.14–1.16, but low K_2O/Na_2O ratios of 0.50–0.70 that agree well with this definition. These characteristics, together with the negative correction between SiO_2 and P_2O_5 (Figure S3f), low zircon saturation temperatures of 763–809 °C (Table S3) with the average value of 786 °C similar to those of the unfractionated (781 °C) and fractionated (764 °C) I-type granites from the Lachlan Fold Belt (LFB), Australia [118] and non-M-type granite affinity discussed above, indicate their likely I-type granite attributes.

Several evidences in the following indicate that the BCN and TL granites probably belong to A-type granites: (1) their SiO_2 (69.3 wt.%–71.7 wt.%, with a mean of 70.3 wt.%), total alkali (7.09 wt.%–8.27 wt.%, with a mean of 7.84 wt.%) and CaO (1.44 wt.%–2.25 wt.%, with a mean of 1.78 wt.%) contents resemble those of typical A-type granites (SiO_2 = 70 wt.%, $Na_2O + K_2O$ = 7 wt.%–11 wt.% and CaO < 1.8 wt.% [119]); (2) their high K_2O contents of 3.95 wt.%–5.33 wt.% with an average value of 4.85 wt.% agree with that of A-type granites (4 wt.%–6 wt.% or even higher [120]); (3) A-type granites feature high FeO_T contents

>1.00 wt.%, which is different from that of highly fractionated I-type granites generally <1.00 wt.% [121]. The BCN and TL granites yield high FeO_T contents of 2.34 wt.%–3.73 wt.% similar to A-type granites; (4) their low Al_2O_3/TiO_2 ratios of 22–34 are consistent with that of A-type granites (generally less than 35, [97]); (5) previous studies have shown that A-type granites originate from high-temperature magmas [118,122,123]. The zircon saturation temperatures of the BCN and TL granites ranging from 830 to 869 °C with a mean of 842 °C (Table S3) resemble those of the LFB aluminous A-type granites, Australia (839 °C [118]) and A-type granites in the Middle section of the BNSZ (833 °C [124]), but are much higher than that of the LFB I-type granites (<790 °C [118]). In particular, considering rare inherited source zircons in the samples (Figure S1f,g,h), the initial temperatures of the magmas should be over 842 °C, indicating "hot" granite magmas; (6) the BCN and TL granites have 10,000 × Ga/Al ratios of 2.32–2.97 where the average value of 2.57 is higher than those of I-type (2.1) and S-type (2.28) granites but resembles that of A-type (2.6) granites [102]. In the plots of 10,000 × Ga/Al versus (Zr + Nb + Ce + Y) and Zr (Figure 10), the BCN and TL granites plot in the A-type granite field. Moreover, the weakly peraluminous (Figure 6c) and the presence of abundant perthites and interstitial hornblendes (Figure 3c–h) reveal that the BCN and TL granites belong to aluminous A-type granites. Note that these granites yield low FeO_T/MgO ratios of 3.06–4.80, which are obviously lower than that of A-type granites (>10 [102]; >16 [104]). Combined with their different chondrite-normalized REE patterns and primitive mantle-normalized element spider diagrams from those of A-type granites which are apparently depleted in Eu ($Eu/Eu^* < 0.30$) and Sr (<100 ppm) [120] (Figure 7), these features imply that the BCN and TL granites may be untypical A-type granites.

In Figure S3, the BCD, BCN and TL granitic samples exhibit clear negative correlations of MgO, Al_2O_3, Fe_2O_{3T}, CaO, TiO_2, Zr and V with SiO_2. These signatures, together with the variable depletions in Eu, Sr and Ti shown in Figure 7e–j, suggest the removal of plagioclase, K–feldspar, hornblende, Fe–Ti oxides and zircon during the evolution of magmas. Note that the BCD granites show no or weak Eu and Sr anomalies compared to the BCN and TL granites (Figure 7e,f), reflecting that plagioclase may have played a lesser role in their magma evolution. In addition, the BCD, BCN and TL granites display strongly fractionated REE patterns (Figure 7e,g,i) with high $(La/Yb)_N$ (14.70–42.80) and $(Dy/Yb)_N$ (1.17–1.65) ratios, which are indicative of residual garnet in the source regions during melting. These rocks have the average $(Dy/Yb)_N$ ratios of 1.36, 1.53 and 1.56, respectively, suggesting that the BCN and TL granites may be derived from a relatively deeper source with more residual garnets than the BCD granites and the Yilashan granophyres (1.18) and quartz diorite–porphyrites (1.20).

BCD I-Type Granite

Three petrogenetic models are provided about the origin of I-type granite magmas that include: (1) the partial melting of mafic to intermediate lower crust [3,70,93,125,126]; (2) the assimilation and fractional crystallization of mantle-derived magmas, with or without crustal contamination [127,128]; and (3) the partial melting of supracrustal sedimentary rocks with the input of mantle-derived melts [129,130]. The BCD granitic samples yield multi-stage zircon U–Pb ages (Table S1), a wide range of zircon $\varepsilon_{Hf}(t)$ values of −8.8 to +2.5 (Figure 5) with T_{DM2} ages of 1.01–1.73 Ga (Table S2) and low $\varepsilon_{Nd}(t)$ values of −11.23 to –7.97 (Figure 8) with T_{DM} ages of 1.29–1.74 Ga (Table S3), suggesting that the BCD granites were likely derived from Paleo–Mesoproterozoic crust with some contribution of mantle-derived magmas and crustal assimilation (see Section 6.1). Several evidences below confirm that mantle-derived melts could not be a dominant factor in the origin of the BCD granites: (1) felsic rocks have high SiO_2 contents >66 wt.% that cannot be derived from the direct partial melting of the mantle source, which would result in the magmas having no more silicic than andesitic in compositions [131–133]; (2) mafic magmas that have undergone progressive fractional crystallization would produce voluminous mafic–ultramafic cumulates that contrast with that of wide granitoids exposed in the study area [109,126,134];

(3) the BCD granites are peraluminous (Figure 6c), which are different from that of magmas generated related to fractional crystallization of mantle-derived magmas, which usually show peralkaline attributes [118,135,136]. Obviously input of mantle derived materials would significantly change the peraluminous features of magmas [114,115]; (4) low MgO (0.54 wt.%–0.93 wt.%), Cr (5.41–12 ppm) and Ni (2.8–5.17 ppm) values and various Nd and zircon Hf isotopic compositions (Tables S2 and S3) and the absence of mafic enclave in rocks.

CaO/Na_2O ratios are often used to determine the compositions of magma sources of granitoid that the ratios < 0.5 indicate pelite-derived magmas, whereas those between 0.3 and 1.5 show magmas derived from graywacke or igneous sources [94]. The BCD granites have high CaO/Na_2O ratios of 0.49–0.68 with the average value of 0.59, suggesting that they may be derived from the partial melting of graywacke or igneous sources. As shown in Figure 9a, these rocks have low $CaO/(MgO + FeO_T + TiO_2)$, but high $(CaO + MgO + FeO_T + TiO_2)$ values that almost fall into the partial melts from the amphibolite field. This conclusion can also be obtained from Figure 9b. Therefore, the BCD granites were likely derived from the partial melting of an amphibolitic/or metabasaltic magma source [95]. In addition, magmas originated from the partial melting of supracrustal sediments are strongly peraluminous [137]. The BCD granites are weakly to obviously peraluminous (Figure 6c), and one sample (BCD–2) plot near the global subducting sediment (GLOSS) field in Figure 8. These signatures, combined with one sample (BCD–4) plotting in the graywacke field in Figure 9a, suggest that the BCD granites may be formed with some influences of sediments.

BCN and TL Untypical A-Type Granites

Three genetic models about A-type granites have generally been invoked that include: (1) the extreme fractional crystallization of mantle-derived basaltic magmas, having or not having crustal contamination [127,138–140]; (2) the partial melting of crustal rocks [98,104, 118,123,135]; and (3) mixing magmas originated from the two end members above [141,142]. Several evidences below reveal that the BCN and TL granites likely have a crustal source. (1) They have high SiO_2 contents >66 wt.% and are peraluminous (Figure 6c); (2) they have low Nb/Ta ratios of 11.76–13.18 with a mean of 12.56 that resemble those of magmas originated from crust (11–12), but are distinct from that of melts derived from mantle (17.5 [143]); (3) their Ce/Pb ratios of 1.91–4.85 (with a mean of 3.01) are closer to that of crust (3.9 [2]) than that of mantle-derived melts (27 [144]); (4) the absence of coeval voluminous mafic magmatism or related intermediate products of crystallization evolution in the study area. The multi-stage zircon U–Pb ages (Table S1) and various $\varepsilon_{Nd}(t)$ (−11.31 to −10.88) and zircon ε_{Hf} (−14.6 to −5.9; crystallization ages) values (Figures 5 and 8) with old Nd T_{DM} (1.38–1.63 Ga) and zircon Hf T_{DM2} (1.54–2.09 Ga) ages (Tables S2 and S3) of the samples show that they were likely derived from Paleo–Mesoproterozoic (dominated by Paleoproterozoic) crust, with crustal assimilation (see Section 6.1) and the contribution of minor mantle-derived melts. The addition of limited mantle-derived magmas is supported by the fact that the BCN and TL granites show high SiO_2 and low MgO, Cr and Ni contents (Table S3) and are peraluminous (Figure 6c).

With regard to crustal origin, the BCN and TL granites are weakly peraluminous with limited influences of mantle-derived melts that are inconsistent with the metasedimentary rock-derived melts, which show apparent peraluminous characteristics [145,146]. Thus, the possibility of a metasedimentary source should be excluded. In Figure 9a, the BCN and TL granites display low $CaO/(MgO + FeO_T + TiO_2)$, but high $(CaO + MgO + FeO_T + TiO_2)$ values that fall into the partial melts from the amphibolite field. This conclusion can also be drawn from Figure 9b. These features are indicative that the BCN and TL granites were likely derived from the partial melting of an amphibolitic/or metabasaltic magma source, resembling that of the BCD granites. In fact, previous studies have shown that the magma sources of I- and A-type composite granites can be similar, and their differences in magma source compositions could be related to the amount of the involvement of mantle-derived

magmas [147]. Note that the BCN and TL granites have higher Y and Yb values than the BCD granites and show observed Eu anomalies (Figure 7e,g,i), implying that they may have a relatively shallower magma source than the BCD granites.

6.3. Tectonic Setting and Geodynamic Implications

Granitoids have many tectonic settings, including volcanic arc, collisional, within-plate and ocean-ridge settings [148]. A recent study concluded that granites are developed particularly related to crustal melting at convergent plate margins where crustal materials had experienced thickening, heating and deformation [4]. In this paper, the granitoid samples belong to calc-alkaline and shoshonitic series (Figure 6b) and display enrichment of LREEs and LILEs and depletion of HFSEs (e.g., Nb, Ta, Ti) (Figure 7). These signatures resemble those of arc-like igneous rocks developed in active continental margin settings [149,150]. Two discrimination diagrams are used to determine the tectonic setting of the granitoid samples. On the Y versus Nb diagram (Figure 11a), the samples almost plot in the VAG (volcanic arc granites) + syn–COLG (syn-collisional granites) field with the sample BCN–1 (~121 Ma) in the WPG (within plate granite) field. Meanwhile, these rocks fall around the GCTS (granites from a collisional tectonic setting) field on the Hf–Rb–Ta diagram (Figure 11b). Moreover, as shown above, the BCN and TL granites are aluminous A-type granite. Generally, aluminous A-type granites are considered to be formed in a post-collisional setting [151,152]. These evidences thus imply that the granitoid samples likely have a collision related setting.

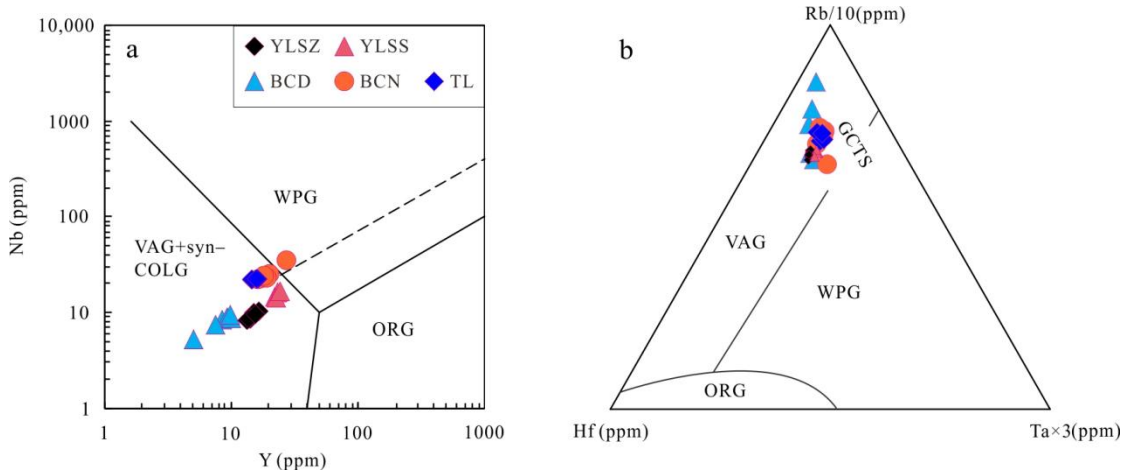

Figure 11. Y versus Nb (**a**) [148] and Rb–Hf–Ta (**b**) [153] diagrams for the Yilashan and Amdo granitoids in the Nagqu area. WPG: within-plate granites; VAG: volcanic arc granites; syn–COLG: syn-collisional granites; ORG: ocean-ridge granites; GCTS: granites from a collisional tectonic setting.

Note that the geochemical features of granites depend mainly upon their magma sources, and there is no direct relationship with the tectonic environment where they are formed. The accurate determination of tectonic setting of granites should be combined with the regional geological background. Although some workers proposed that the collision between the Lhasa and Qiangtang terranes happened prior to Cretaceous [13,154], evidences of magmatism, sedimentary, metamorphism, tectonics and paleolatitude along the BNSZ generally demonstrated that the amalgamating of the Lhasa–Qiangtang terranes likely took place in the Early Cretaceous [15,18–20,22,23,31]. For example, the Lhasa terrane initially collided with the Qiangtang terrane in the Late Jurassic–Early Cretaceous with the time most likely at 140–130 Ma based on the integrated evidences of lithostratigraphy, magmatism and metamorphism of the Lhasa–Qiangtang collision zone [18]. This conclusion is comparable with the Early Cretaceous (>130 Ma) collision constrained by paleolatitude [20], but more evidences are indicative that the Lhasa–Qiangtang collision should have happened later. The collision of the Lhasa and Qiangtang terranes in the Nima

area (Figure 1b) likely happened at 125–118 Ma based on the mapping and geochronology [15]. Recently, the timing of closure of the BNTO was between 124 and 117 Ma and the Lhasa terrane collided with the Qiangtang terrane at 117–115 Ma based on the studies of the Asa Early Cretaceous igneous rocks [23] (Figure 1b). The timing of the Lhasa and Qiangtang collision was ~114 Ma, which is constrained by the Lower Cretaceous Duoni Formation in the Baingoin area [19] (Figure 1b). The initial collision of the Lhasa–Qiangtang terranes had taken place by 122 Ma based on the evidences of Lower Cretaceous strata in the Baingoin basin [22]. In addition, previous studies of zircon U–Pb dating revealed that the Yilashan ophiolite was developed at ~183–133 Ma [43–46]. These ages are older than those of the granitoid samples (121–108 Ma; Figure 4) reported in this paper. To sum up, we can infer that the Yilashan–Amdo ~121–108 Ma quartz diorite–porphyrites and granites were probably produced related to the Lhasa–Qiangtang collision and the BNTO had been closed during this time in the study area.

Partial melting of source rocks is usually controlled by several factors including temperature increase, pressure decrease and involvement of aqueous fluids. The thermal anomaly triggering partial melting of lower crust can be provided by asthenospheric mantle upwelling or the underplating of mantle-derived melts [155,156]. The asthenospheric upwelling can be induced by some factors including lithospheric extension or the oceanic slab rollback and breakoff. During the subduction process of oceanic slab beneath the continent, due to the continental lithosphere and oceanic lithosphere exhibiting different buoyancy, their contrasting buoyancy will finally lead in the breakoff of subducted slab after continent–continent collision [157,158]. In addition, for S-type granites derived from the partial melting of sedimentary rocks, their source rocks must be buried and then metamorphosed to trigger dehydration melting at elevated P–T conditions [118]. Previous studies have also shown that S-type granites are usually produced by the partial melting of sedimentary rocks during accretionary orogeny [159,160]. In this paper, the YLSS S-type granophyres (~112 Ma) were developed by partial melting of a graywacke source related to the Lhasa–Qiangtang collision following the closure of the BNTO. During this process, accompanied by the underthrusting of the Lhasa terrane underneath the (Amdo–) southern Qiangtang terrane (Figure 12) driven by the continued northward subduction of the Yarlung Zangbo Tethys Ocean beneath the Lhasa terrane to the south [15], graywackes preserved within the accretionary wedge were dragged into the lower crust to undergo metamorphism. On the other hand, the BCN and TL A-type granites have relatively high zircon saturation temperatures (830–869 °C; Table S3), suggesting that they were derived from a relatively refractory source under relatively high temperatures associated with mantle upwelling or mafic magma inrush into a localized area. However, plume-related A-type granites generated at high temperatures differ from the BCN and TL A-type granites, which display zircon saturation temperatures less than 900 °C [139,161] that this genetic model should be excluded. This model is also against their Nd–Hf isotopic compositions. Thus, the development of ~121–110 Ma BCN and TL A-type granites probably indicate a stage of structural transformation from collisional extrusion to extension with related lithospheric thinning and asthenospheric upwelling. During the late Early Cretaceous, BNTO plate continued to subduct beneath the Qiangtang terrane after the earlier collision of the Lhasa–Qiangtang terranes, and the slab breakoff at ~121–110 Ma to trigger intensive asthenospheric upwelling and subsequent mantle-derived magmas underplating into the lower crust (Figure 12). The underplating of mantle-derived melts provided heat for partial melting of the Paleo–Mesoproterozoic lower crustal mafic rocks and the deep buried graywackes to produce the Amdo granites (~121–110 Ma; BCD, BCN and TL), the YLSZ quartz diorite–porphyrites (~109–108 Ma) and the YLSS granophyres (~112 Ma), respectively. In addition, as discussed above, a small amount of mantle-derived melts had been involved in the generation of the YLSZ quartz diorite–porphyrite and the Amdo granites. This means that the underplating of mantle-derived magmas not only provided heat for partial melting of the lower crust but also directly brought a certain amount of mantle-derived components to the source regions. However, we cannot exclude the

possibility that the mantle-derived materials involved in the formation of the granitoid samples were derived from juvenile crust.

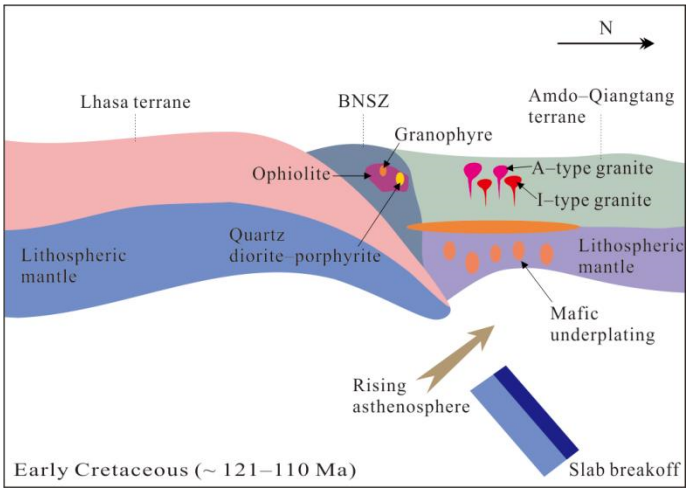

Figure 12. A simplified geodynamic model for the Yilashan and Amdo Early Cretaceous granitoids. Not drawn to scale. The Yilashan and Amdo granitoids were formed related to the Lhasa–Qiangtang collision during the late Early Cretaceous (~121–110 Ma) associated with the northward subducted slab breakoff of the Bangong–Nujiang Tethys Ocean beneath the southern Qiangtang (–Amdo) terrane. The partial melting of the lower crustal source rocks was triggered by asthenospheric upwelling.

On the other hand, previous studies have shown that the Yilashan ophiolite was emplaced into the Jurassic Yilashan Formation (JM*y*), which belongs to the Jurassic Mugagangri Group (JM) (Figure 1c [33]). In view of that, the Yilashan ophiolite has multiple formation ages ranging from ~184 to 133 Ma [43–46], the time of its tectonic emplacement should be after ~133 Ma. Note that only local Late Cretaceous but no Early Cretaceous intermediate-felsic igneous rocks occur within the Jurassic Mugagangri Group (JM*y*, JM*b*), which contact with the Yilashan ophiolite (Figure 1c [33]). If the Yilashan ophiolite was intruded by the Early Cretaceous granophyric and quartz diorite–porphyritic intrusions after its earlier emplacement into the Jurassic Yilashan Formation (JM*y*), why are there no coeval Early Cretaceous intermediate-felsic intrusions within the Jurassic Mugagangri Group (JM*y*, JM*b*)? Thus, it is possible that the Yilashan ophiolite was intruded by the ascending of Early Cretaceous intermediate-felsic magmas to form the granophyric and quartz diorite–porphyritic intrusions at ~112–108 Ma at a certain stage of emplacement somewhere, and finally, all of them were emplaced into the Jurassic Yilashan Formation (JM*y*) because of the intensifying collision orogenesis.

7. Conclusions

1. The Yilashan and Amdo granitoid samples were formed at ~121–110 Ma related to the collision between the Lhasa and southern Qiangtang (–Amdo) terranes. The BNTO was closed during this period in the study area.
2. The Yilashan S-type granophyres were derived from partial melting of a Paleoproterozoic metagraywacke source in the lower crust. The Yilashan quartz diorite–porphyrites and the Amdo I-type granites were mainly originated from partial melting of Paleo–Mesoproterozoic lower crustal mafic rocks involved with a small amount of components derived from the Amdo orthogneisses and mantle-derived magmas. The Amdo A-type granites were mainly derived from a Paleo–Mesoproterozoic (dominated by Paleoproterozoic) source composed of metabasaltic rocks along with the insignificant input of mantle-derived melts. A Precambrian "hidden" crust likely existed beneath the northern Lhasa and Amdo blocks.

3. The underplating of mantle-derived melts related to asthenospheric upwelling not only provided sufficient heat for partial melting of crustal sources at various levels but also led to crustal-derived melts to mix with mantle-derived materials (the YLSZ quartz diorite–porphyrite and the Amdo granites).
4. The Yilashan ophiolite was intruded by the Early Cretaceous (~112–108 Ma) granophyric and quartz diorite–porphyritic intrusions prior to its final tectonic emplacement into the surrounding Jurassic strata.

Supplementary Materials: The following supporting information can be downloaded at: https://www.mdpi.com/article/10.3390/min12080933/s1, Figure S1. Cathodoluminescence images of the analyzed zircons from the Yilashan and Amdo granitoids in the Nagqu area. Figure S2. the YLSZ quartz diorite–porphyrites generally show negative correlations of MgO (a), Al_2O_3(b), Fe_2O_3T(c), TiO_2(d), P_2O_5(e), CaO (f), Ni (g), Zr (h) and V (i) with SiO_2. Figure S3. the BCD, BCN and TL granitic samples exhibit clear negative correlations of MgO (a), Al_2O_3(b), Fe_2O_3T(c), TiO_2(d), P_2O_5(e), CaO (f), Ni (g), Zr (h) and V (i) with SiO_2. Table S1. Zircon LA–ICP–MS U–Pb isotopic data for the Yilashan and Amdo granitoids in the Nagqu area. Table S2. Zircon Lu–Hf isotopic data for the Yilashan and Amdo granitoids in the Nagqu area. Table S3. Whole-rock major (wt.%), trace element (ppm) and Sr–Nd isotopic data for the Yilashan and Amdo granitoids in the Nagqu area.

Author Contributions: Conceptualization, K.W., Y.Z. and Y.Y.; methodology, K.W., Y.Z. and Y.Y.; software, K.W. and Y.Y.; validation, K.W., Y.Z. and Y.Y.; formal analysis, K.W., Y.Z. and Y.Y.; investigation, Y.Z.; resources, Y.Z. and Z.W.; data curation, K.W. and Y.Y.; writing—original draft preparation, K.W.; writing—review and editing, Y.Y.; visualization, K.W., Y.Z., Y.Y. and T.W.; supervision, Y.Y.; project administration, B.X.; funding acquisition, Y.Y. and B.X. All authors have read and agreed to the published version of the manuscript.

Funding: This work was supported by the National Nature Science Foundation of China (grant 42102256); the Nature Science Foundation of Guangdong Province (grant 2018B030311030); and Tibetan Special Foundation of China Geological Survey (grant 1212011221105).

Data Availability Statement: Data is available on request from the corresponding author of the manuscript.

Acknowledgments: We acknowledge Wei Huang and Zheng–Xin Yin for their help in field work and Guo–Qing Zhou, Liang Qi and Lian Zhou for their analytical assistance.

Conflicts of Interest: The authors declare no conflict of interest.

References

1. Pitcher, W.S. *The Nature and Origin of Granite*; Springer: Dordrecht, The Netherlands, 1997; Volume 14, pp. 288–294.
2. Rudnick, R.; Gao, S. The role of lower crustal recycling in continent formation. *Geochim. Et Cosmochim. Acta* **2003**, *67*, 43.
3. Gao, P.; Zheng, Y.F.; Zhao, Z.F. Experimental melts from crustal rocks: A lithochemical constraint on granite petrogenesis. *Lithos* **2016**, *266–267*, 133–157. [CrossRef]
4. Hopkinson, T.N.; Harris, N.B.W.; Warren, C.J.; Spencer, C.J.; Roberts, N.M.W.; Horstwood, M.S.A.; Parrish, R.R. EIMF. The identification and significance of pure sediment–derived granites. *Earth Planet Sci. Lett.* **2017**, *467*, 57–63. [CrossRef]
5. Xu, C.; Yuan, Y.J.; Xiao, Y.; Guo, F.; Xia, B.; Lu, Y. Geochemistry and Geochronology of the Cenozoic Zhalaga Granitoids of the Yulong Alkali-rich Porphyry Belt in Eastern Tibet (Xizang), SW China: Petrogenesis and Tectonic Implications. *Acta Geol. Sin-Engl.* **2020**, *94*, 2077–2090.
6. Yuan, Y.J.; Zhong, Y.; Guo, F.; Xia, B.; Zhang, Y.Q. Geochemical and geochronological constraints on the genesis of Pliocene post–collisional granite porphyry and shoshonite in Quanshuigou, western Kunlun Mountains, NW Qinghai–Tibet Plateau. *Int. Geol. Rev.* **2022**, *64*, 275–296. [CrossRef]
7. Zhu, D.C.; Mo, X.X.; Niu, Y.; Zhao, Z.D.; Wang, L.Q.; Liu, Y.S.; Wu, F.Y. Geochemical investigation of Early Cretaceous igneous rocks along an east–west traverse throughout the central Lhasa Terrane, Tibet. *Chem. Geol.* **2009**, *268*, 298–312. [CrossRef]
8. Zhu, D.C.; Zhao, Z.D.; Niu, Y.; Mo, X.X.; Chung, S.L.; Hou, Z.Q. The Lhasa Terrane: Record of a microcontinent and its histories of drift and growth. *Earth Planet Sci. Lett.* **2011**, *301*, 241–255. [CrossRef]
9. Zhu, D.C.; Zhao, Z.D.; Niu, Y.L.; Dilek, Y.; Hou, Z.Q.; Mo, X.X. The origin and pre–Cenozoic evolution of the Tibetan Plateau. *Gondwana Res.* **2013**, *23*, 1430–1455. [CrossRef]
10. Ji, W.Q.; Wu, F.Y.; Chung, S.L.; Li, J.X.; Liu, C.Z. Zircon U–Pb chronology and Hf isotopic constraints on the petrogenesis of Gangdese batholiths, southern Tibet. *Chem. Geol.* **2009**, *262*, 229–245. [CrossRef]

11. Liu, D.L.; Shi, R.D.; Ding, L.; Huang, Q.S.; Zhang, X.R.; Yue, Y.H.; Zhang, L.Y. Zircon U–Pb age and Hf isotopic compositions of Mesozoic granitoids in southern Qiangtang, Tibet: Implications for the subduction of the Bangong–Nujiang Tethyan ocean. *Gondwana Res.* **2017**, *41*, 157–172. [CrossRef]
12. Xu, R.H.; Schärer, U.; Allègre, C.J. Magmatism and metamorphism in the Lhasa block (Tibet): A chronological study. *J. Geol.* **1985**, *93*, 41–57. [CrossRef]
13. Ma, A.; Hu, X.M.; Garzanti, E.; Han, Z.; Lai, W. Sedimentary and tectonic evolution of the southern Qiangtang basin: Implications for the Lhasa–Qiangtang collision timing: Mesozoic geology of central Tibet. *J. Geophys. Res. Solid Earth* **2017**, *122*, 4790–4813. [CrossRef]
14. Ratschbacher, L.; Frisch, W.; Liu, G.; Chen, C. Distributed deformation in southern and western Tibet during and after the India–Asia collision. *J. Geophys. Res. Solid Earth* **1994**, *99*, 19917–19945. [CrossRef]
15. Kapp, P.; DeCelles, P.G.; Gehrels, G.E.; Heizler, M.; Ding, L. Geological records of the Lhasa–Qiangtang and Indo–Asian collisions in the Nima area of central Tibet. *Geol. Soc. Am. Bull.* **2007**, *119*, 917–933. [CrossRef]
16. Raterman, N.S.; Robinson, A.C.; Cowgill, E.S. Structure and detrital zircon geochronology of the Domar fold–thrust belt: Evidence of pre–Cenozoic crustal thickening of the western Tibetan Plateau. *Spec. Pap. Geol. Soc. of Am.* **2014**, *507*, 89–114.
17. Chen, S.S.; Shi, R.D.; Zou, H.B.; Huang, Q.S.; Liu, D.L.; Gong, X.H.; Yi, G.D.; Wu, K. Late Triassic Island–arc–back–arc basin development along the Bangong–Nujiang suture zone (central Tibet): Geological, geochemical and chronological evidence from volcanic rocks. *Lithos* **2015**, *230*, 30–45. [CrossRef]
18. Zhu, D.C.; Li, S.M.; Cawood, A.; Wang, Q.; Zhao, Z.D.; Liu, S.A.; Wang, L.Q. Assembly of the Lhasa and Qiangtang terranes in central Tibet by divergent double subduction. *Lithos* **2016**, *245*, 7–17. [CrossRef]
19. Zhu, Z.C.; Zhai, Q.G.; Hu, P.Y.; Tang, Y.; Wang, H.T.; Wang, W.; Hao, W.; Huang, Z.Q. Timing of the Lhasa–Qiangtang Collision: Constraints from the sedimentary records of the Duoni Formation from the middle segment of the Bangong–Nujiang suture zone. *Acta Sediment. Sinica* **2020**, *38*, 712–726, (In Chinese with English Abstract).
20. Bian, W.W.; Yang, T.S.; Ma, Y.M.; Jin, J.J.; Gao, F.; Zhang, S.H.; Wu, H.C.; Li, H.Y. New Early Cretaceous palaeomagnetic and geochronological results from the far western Lhasa terrane: Contributions to the Lhasa–Qiangtang collision. *Sci. Rep. UK* **2017**, *7*, 16216. [CrossRef]
21. Fan, J.J.; Li, C.; Liu, J.H.; Wang, M.; Liu, Y.M.; Xie, C.M. The Middle Triassic evolution of the Bangong–Nujiang Tethyan Ocean: Evidence from analyses of OIB–type basalts and OIB–derived phonolites in northern Tibet. *Int. J. Earth Sci.* **2017**, *107*, 1755–1775. [CrossRef]
22. Lai, W.; Hu, X.M.; Garzanti, E.; Xu, Y.W.; Ma, A.L.; Li, W. Early Cretaceous sedimentary evolution of the northern Lhasa terrane and the timing of initial Lhasa–Qiangtang collision. *Gondwana Res.* **2019**, *73*, 136–152. [CrossRef]
23. Wang, W.; Wang, M.; Zhai, Q.G.; Xie, C.M.; Hu, P.Y.; Li, C.; Liu, J.H.; Luo, A.B. Transition from oceanic subduction to continental collision recorded in the Bangong–Nujiang suture zone: Insights from Early Cretaceous magmatic rocks in the north–central Tibet. *Gondwana Res.* **2020**, *78*, 77–91. [CrossRef]
24. Wang, S.; Yang, T.S.; Gao, F.; Bian, W.W.; Jin, J.J.; Peng, W.X.; Jiao, X.W.; Ma, J.H.; Zhang, S.H.; Wu, H.C.; et al. Paleomagnetic and geochronological results of the Risong formation in the western Lhasa terrane: Insights into the Lhasa-Qiangtang collision and stratal age. *Palaeogeogr. Palaeocl.* **2022**, *586*, 110778. [CrossRef]
25. Bao, S.; Xiao, X.C.; Su, L.; Wang, J. Geochemical characteristics and isotopic dating for the Dongcuo ophiolite, Tibet Plateau. *Sci. China Earth Sci.* **2007**, *50*, 660–671. [CrossRef]
26. Zhang, Y.X.; Li, Z.W.; Yang, W.G.; Zhu, L.D.; Jin, X.; Zhou, X.Y.; Tao, G.; Zhang, K.J. Late Jurassic–Early Cretaceous episodic development of the Bangong Meso–Tethyan subduction: Evidence from elemental and Sr–Nd isotopic geochemistry of arc magmatic rocks, Gaize region, central Tibet, China. *J. Asian Earth Sci.* **2017**, *135*, 212–242. [CrossRef]
27. Liu, W.L.; Huang, Q.T.; Gu, M.; Zhong, Y.; Zhou, R.J.; Gu, X.D.; Zheng, H.; Liu, J.N.; Lu, X.X.; Xia, B. Origin and tectonic implications of the Shiquanhe high–Mg andesite, western Bangong suture, Tibet. *Gondwana Res.* **2018**, *60*, 1–14. [CrossRef]
28. Cao, Y.; Sun, Z.; Li, H.; Ye, X.; Yang, Z. Paleomagnetism and U-Pb geochronology of early Cretaceous volcanic rocks from the Qiangtang block, tibetan plateau: Implications for the Qiangtang-Lhasa collision. *Tectonophysics* **2020**, *789*, 228500. [CrossRef]
29. Fan, J.J.; Niu, Y.; Liu, Y.M.; Hao, Y.J. Timing of closure of the Meso-Tethys ocean: Constraints from remnants of a 141–135 ocean island within the bangong-nujiang suture zone, Tibetan Plateau. *Geol. Soc. Am. Bull.* **2021**, *133*, 1875–1889. [CrossRef]
30. Shuai, X.; Li, S.M.; Zhu, D.C.; Wang, Q.; Zhao, Z. Tetrad effect of rare earth elements caused by fractional crystallization in high-silica granites: An example from central tibet. *Lithos* **2021**, *384–385*, 105968. [CrossRef]
31. Yin, A.; Harrison, T.M. Geologic evolution of the Himalayan–Tibetan orogen. *Annu. Rev. Earth Planet. Sci.* **2000**, *28*, 211–280. [CrossRef]
32. Fan, J.J.; Li, C.; Wang, M.; Xie, C.M. Reconstructing in space and time the closure of the middle and western segments of the Bangong–Nujiang Tethyan Ocean in the Tibetan Plateau. *Int. J. Earth Sci.* **2018**, *107*, 231–249. [CrossRef]
33. Xizang Geological Survey Institute. The regional geological survey of Nagqu Sheet. scale 1:500,000, 1 sheet. 2005; *unpublished*. (In Chinese)
34. China University of Geosciences (Beijing). The regional geological survey of 1: 250,000 Amdo Sheet. 2005; *unpublished*. (In Chinese)
35. Zhang, Z.M.; Dong, X.; Liu, F.; Lin, Y.H.; Yan, R.; Santosh, M. Tectonic evolution of the Amdo terrane, central Tibet: Petrochemistry and zircon U–Pb geochronology. *J. Geol.* **2012**, *120*, 431–451. [CrossRef]

36. Harris, N.B.W.; Holland, T.J.B.; Tindle, A.G. Metamorphic rocks of the 1985 Tibet Geotraverse, Lhasa to Golmud. *Philos. Trans. R. Soc. Lond.* **1988**, *327*, 203–213.
37. Guynn, J.; Kapp, P.; Gehrels, G.E.; Ding, L. U–Pb geochronology of basement rocks in central Tibet and paleogeographic. *J. Asian Earth Sci.* **2012**, *43*, 23–50. [CrossRef]
38. Guynn, J.; Tropper, P.; Kapp, P.; Gehrels, G.E. Metamorphism of the Amdo metamorphic complex, Tibet: Implications for the Jurassic tectonic evolution of the Bangong suture zone. *J. Metamorph. Geol.* **2013**, *31*, 705–727. [CrossRef]
39. Lu, L.; Wu, Z.H.; Zhao, Z.; Hu, D.G.; Ye, P.S. Zircon SHRIMP U–Pb dating, geochemical characteristics and tectonic significance of granitic gneisses in Amdo, Tibet. *J. Earth Sci. China* **2014**, *25*, 473–485. [CrossRef]
40. Lu, L.; Qian, C.; Zhao, Z.; Wu, Z.; Liu, Y.; Zhou, L.; Wang, Y. Geochronological evidence of Ordovician and Jurassic magmatic events in Nyainrong microcontinent, Tibet. *Earth Sci.* **2018**, *43*, 1110–1124, (In Chinese with English Abstract).
41. Zhang, X.R.; Shi, R.D.; Huang, Q.S.; Liu, D.L.; Gong, X.H.; Chen, S.S.; Wu, K.; Yi, G.D.; Sun, Y.L.; Ding, L. Early Jurassic high–pressure metamorphism of the Amdo terrane, Tibet: Constraints from zircon U–Pb geochronology of mafic granulites. *Gondwana Res.* **2014**, *26*, 975–985. [CrossRef]
42. Dai, J.G.; Wang, C.S.; Hourigan, J.K.; Santosh, M. Insights into the early Tibetan Plateau from (U–Th)/He thermochronology. *J. Geol. Soc. Lond.* **2013**, *170*, 917–927. [CrossRef]
43. Huang, Q.S.; Shi, R.D.; Liu, D.L.; Zhang, X.R.; Fan, S.Q.; Ding, L. Os isotopic evidence for a carbonaceous chondritic mantle source for the Nagqu ophiolite from Tibet and its implications. *Chin. Sci. Bull.* **2013**, *58*, 92–98, (In Chinese with English Abstract). [CrossRef]
44. Yin, Z.X.; Yuan, Y.J.; LÜ, B.F.; Cai, Z.R.; Zheng, H.; Huang, Q.T.; Xia, B.; Zhong, Y.; Xia, Z.Y.; Shi, X.L.; et al. Zircon U–Pb Geochronology and Hf Isotopic Constraints on Petrogenesis of Plagiogranite from the Cuomuqu Ophiolite, Bangong Lake Area, North Tibet. *Acta Geol. Sin-Engl.* **2015**, *89*, 418–440.
45. Zhong, Y.; Hu, X.C.; Liu, W.L.; Xia, B.; Zhang, X.; Huang, W.; Fu, Y.B.; Wang, Y.G. Age and nature of the Jurassic–Early Cretaceous mafic and ultramafic rocks from the Yilashan area, Bangong–Nujiang suture zone, central Tibet: Implications for petrogenesis and tectonic Evolution. *Int. Geol. Rev.* **2017**, *60*, 1244–1266. [CrossRef]
46. Zhang, R. The Feature and Tectonic Setting of Chromitite from the Yilashan Ophiolite in Middle Section of Bangong–Nujiang Suture Zone, Tibet. Master's Thesis, Chinese Academy of Geological Sciences, Beijing, China, 2020; pp. 1–92. (In Chinese with English Abstract)
47. Garzanti, E.; Le Fort, P.; Sciunnach, D. First report of Lower Permian basalts in South Tibet: Tholeiitic magmatism during break–up and incipient opening of Neotethys. *J. Asian Earth Sci.* **1999**, *17*, 533–546. [CrossRef]
48. Stampfli, G.M. Tethyan oceans. *Geol. Soc. Lond. Spec. Publ.* **2000**, *173*, 1–23. [CrossRef]
49. Zhang, K.J.; Cai, J.X.; Zhang, Y.X.; Zhao, T.P. Eclogites from central Qiangtang, northern Tibet (China) and tectonic implications. *Earth Planet Sci. Lett.* **2006**, *245*, 722–729. [CrossRef]
50. Schneider, W.; Mattern, F.; Wang, P.; Li, C. Tectonic and sedimentary basin evolution of the eastern Bangong–Nujiang zone (Tibet): A Reading cycle. *Int. J. Earth Sci.* **2003**, *92*, 228–254. [CrossRef]
51. Pullen, A.; Kapp, P.; Gehrels, G.E.; Ding, L.; Zhang, Q. Metamorphic rocks in central Tibet: Lateral variations and implications for crustal structure. *Geol. Soc. Am. Bull.* **2011**, *123*, 585–600. [CrossRef]
52. Zhang, K.J.; Zhang, Y.X.; Tang, X.C.; Xia, B. Late Mesozoic tectonic evolution and growth of the Tibetan plateau prior to the Indo–Asian collision. *Earth Sci. Rev.* **2012**, *14*, 236–249. [CrossRef]
53. Hao, L.L.; Wang, Q.; Wyman, D.A.; Quan, O.; Dan, W.; Jiang, Z.Q.; Wu, F.Y.; Yang, J.S.; Long, X.P.; Li, J. Underplating of basaltic magmas and crustal growth in a continental arc: Evidence from Late Mesozoic intermediate–felsic intrusive rocks in southern Qiangtang, central Tibet. *Lithos* **2015**, *245*, 223–242. [CrossRef]
54. Hou, Z.Q.; Duan, L.F.; Lu, Y.J.; Zheng, Y.C.; Zhu, D.C.; Yang, Z.M.; Yang, Z.S.; Wang, B.D.; Pei, Y.R.; Zhao, Z.D.; et al. Lithospheric architecture of the Lhasa terrane and its control on ore deposits in the Himalayan–Tibetan orogen. *Econ. Geol.* **2015**, *110*, 1541–1575. [CrossRef]
55. Liu, D.L.; Shi, R.D.; Ding, L.; Zou, H.B. Late Cretaceous transition from subduction to collision along the Bangong–Nujiang Tethys: New volcanic constraints from central Tibet. *Lithos* **2018**, *296–299*, 452–470. [CrossRef]
56. Sui, Q.L.; Wang, Q.; Zhu, D.C.; Zhao, Z.D.; Chen, Y.; Santosh, M.; Hu, C.Z.; Yuan, H.L.; Mo, X.X. Compositional diversity of ca. 110 Ma magmatism in the northern Lhasa Terrane, Tibet: Implications for the magmatic origin and crustal growth in a continent–continent collision zone. *Lithos* **2013**, *168–169*, 144–159. [CrossRef]
57. Xiao, X.C.; Li, Y.D. *Tectonic and Evolution and Uplift of Qinghai–Xizang (Tibet) Plateau*; Guangdong Science and Technology Press: Guangzhou, China, 2000; pp. 1–313, (In Chinese with English abstract).
58. Zhong, Y.; Liu, W.L.; Xia, B.; Liu, J.N.; Guan, Y.; Huang, W.; Sun, X.M. Geochemistry and geochronology of the Mesozoic Lanong ophiolitic mélange, northern Tibet: Implications for petrogenesis and tectonic evolution. *Lithos* **2017**, *292–293*, 111–131. [CrossRef]
59. Wang, B.D.; Wang, L.Q.; Chung, S.L.; Chen, J.L.; Yin, F.G.; Liu, H.; Li, X.B.; Chen, L.K. Evolution of the Bangong–Nujiang Tethyan ocean: Insights from the geochronology and geochemistry of mafic rocks within ophiolites. *Lithos* **2016**, *245*, 18–33. [CrossRef]
60. Tang, Y.; Zhai, Q.G.; Hu, P.Y.; Xiao, X.C.; Wang, H.T. Petrology, geochemistry and geochronology of the Zhongcang ophiolite, northern Tibet: Implications for the evolution of the Bangong–Nujiang Ocean. *Geosci. Front.* **2018**, *9*, 1369–1381. [CrossRef]
61. Pan, G.T.; Wang, L.Q.; Li, R.S.; Yuan, S.H.; Ji, W.H.; Yin, F.G.; Zhang, W.P.; Wang, B.D. Tectonic evolution of the Qinghai–Tibet Plateau. *J. Asian Earth Sci.* **2012**, *53*, 3–14. [CrossRef]

62. Coward, M.P.; Kidd, W.F.; Yun, P.; Shackleton, R.M.; Zhang, H. The structure of the 1985 Tibet Geotraverse, Lhasa to Golmud. *Philos. Trans. R. Soc. Lond.* **1988**, *327*, 307–336.
63. Zhang, Z.M.; Dong, X.; Santosh, M.; Zhao, G.C. Metamorphism and tectonic evolution of the Lhasa terrane, Central Tibet. *Gondwana Res.* **2014**, *25*, 170–189. [CrossRef]
64. Shi, R.D.; Griffin, W.L.; O'Reilly, S.Y.; Huang, Q.S.; Zhang, X.R.; Liu, D.L.; Zhi, X.C.; Xia, Q.X.; Ding, L. Melt/mantle mixing produces podiform chromite deposits in ophiolites: Implications of Re–Os systematics in the Dongqiao Neo–Tethyan ophiolite, northern Tibet. *Gondwana Res.* **2012**, *21*, 194–206. [CrossRef]
65. Liu, Y.; Gao, S.; Hu, Z.; Gao, C.; Zong, K.; Wang, D. Continental and oceanic crust recycling–induced melt–peridotite interactions in the Trans–North China Orogen: U–Pb dating, Hf isotopes and trace elements in zircons from mantle xenoliths. *J. Petrol.* **2010**, *51*, 537–571. [CrossRef]
66. Ludwing, K.R. *Isoplot: A Geochronological Toolkit for Microsoft Excel*; Berkeley Geochronology Center Special Publication: Berkeley, CA, USA, 2003; pp. 1–70.
67. Scherer, E.; Münker, C.; Mezger, K. Calibration of the Lutetium–Hafnium Clock. *Science* **2001**, *293*, 683–687. [CrossRef] [PubMed]
68. Blichert, T.J.; Albarede, F. The Lu–Hf geochemistry of the chondrites and the evolution of the mantle–crust system. *Earth Planet Sci. Lett.* **1997**, *148*, 243–258. [CrossRef]
69. Griffin, W.L.; Belousova, E.A.; Shee, S.R.; Pearson, N.J.; O'Reilly, S.Y. Archean crustal evolution in the northern Yilgarn Craton: U–Pb and Hf–isotope evidence from detrital zircons. *Precambrian Res.* **2004**, *131*, 231–282. [CrossRef]
70. Griffin, W.L.; Wang, X.; Jackson, S.E.; Pearson, N.J.; O'Reilly, S.Y.; Xu, X.S.; Zhou, X.M. Zircon chemistry and magma mixing, SE china: In–situ analysis of Hf isotopes, Tonglu and Pingtan igneous complexes. *Lithos* **2002**, *61*, 237–269. [CrossRef]
71. Morel, M.L.A.; Nebel, O.; Nebel–Jacobsen, Y.J.; Miller, J.S.; Vroon, P.Z. Hafnium isotope characterization of the GJ–1 zircon reference material by solution and laser–ablation MC–ICPMS. *Chem. Geol.* **2008**, *255*, 231–235. [CrossRef]
72. Wu, F.Y.; Li, X.H.; Zheng, Y.F.; Gao, S. Lu–Hf isotopic systematics and their applications in petrology. *Acta Petrol. Sin.* **2006**, *23*, 185–220, (In Chinese with English Abstract).
73. Hou, K.J.; Li, Y.H.; Zou, T.R.; Qu, X.M.; Shi, Y.R.; Xie, G.Q. Laser ablation–MC–ICP–MS technique for Hf isotope microanalysis of zircon and its geological applications. *Acta Petrol. Sin.* **2007**, *23*, 2595–2604, (In Chinese with English Abstract).
74. Chen, L.; Zhao, Z.F.; Zheng, Y.F. Origin of andesitic rocks: Geochemical constraints from Mesozoic volcanics in the Luzong basin, South China. *Lithos* **2014**, *190–191*, 220–239. [CrossRef]
75. Gao, S.; Lin, W.L.; Qiu, Y.; Zhou, L.; Hartmann, G.; Simon, K. Contrasting geochemical and Sm–Nd isotopic compositions of Archean metasediments from the Kongling high–grade terrain of the Yangtze craton: Evidence for cratonic evolution and redistribution of REE during crustal anatexis. *Geochim. Cosmochim. Acta* **1999**, *63*, 2071–2088. [CrossRef]
76. Le Maitre, R.W.; Bateman, P.; Dudek, A.; Keller, J.; Lameyre, J.; Le Bas, M.J.; Sabine, P.A.; Schmid, R.; Sorensen, H.; Streckeisen, A.; et al. *A Classification of Igneous Rocks and Glossary of Terms: Recommendations of the International Union of Geological Sciences Subcommission on the Systematics of Igneous Rocks*; Blackwell: Oxford, UK, 1989.
77. Peccerillo, A.; Taylor, S.R. Geochemistry of Eocene calc–alkaline volcanic rocks from the Kastamonu area, northern Turkey. *Contrib. Mineral Petr.* **1976**, *58*, 63–81. [CrossRef]
78. Maniar, P.D.; Piccoli, P.M. Tectonic discrimination of granitoids. *Geol. Soc. Am. Bull.* **1989**, *101*, 635–643. [CrossRef]
79. Sun, S.S.; McDonough, W.F. Chemical and isotopic systematics of oceanic basalt: Implication for mantle composition and processes. *Geol. Soc. Lond. Spec. Publ.* **1989**, *42*, 528–548. [CrossRef]
80. Lai, S.C.; Qin, J.F.; Li, Y.F. Partial melting of thickened Tibetan crust: Geochemical evidence from Cenozoic adakitic volcanic rocks. *Int. Geol. Rev.* **2007**, *49*, 357–373. [CrossRef]
81. Taylor, S.R.; McLennan, S.M. The Continental Crust: Its Composition and Evolution. *J. Geol.* **1985**, *94*, 632–633.
82. Rudnick, R.L.; Fountain, D.M. Nature and composition of the continental crust: A lower crustal perspective. *Rev. Geophys.* **1995**, *33*, 267–309. [CrossRef]
83. Plank, T.; Langmuir, C.H. The chemical composition of subducting sediment and its consequences for the crust and mantle. *Chem. Geol.* **1998**, *145*, 325–394. [CrossRef]
84. Chen, Y.; Zhu, D.C.; Zhao, Z.D.; Meng, F.Y.; Wang, Q.; Santosh, M.; Wang, L.Q.; Dong, G.C.; Mo, X.X. Slab breakoff triggered ca. 113 Ma magmatism around Xainza area of the Lhasa Terrane, Tibet. *Gondwana Res.* **2014**, *26*, 449–463. [CrossRef]
85. Liu, Y.M.; Wang, M.; Li, C.; Xie, C.M.; Chen, H.Q.; Li, Y.B.; Fan, J.J.; Li, X.K.; Xu, W.; Sun, Z.M. Cretaceous structures in the Duolong region of central Tibet: Evidence for an accretionary wedge and closure of the Bangong–Nujiang Neo–Tethys Ocean. *Gondwana Res.* **2017**, *48*, 110–123. [CrossRef]
86. Bea, F.; Fershtater, G.B.; Montero, P.; Whitehouse, M.; Levin, V.Y.; Scarrow, J.H.; Austrheim, H.; Pushkariev, E.V. Recycling of continental crust into the mantle as revealed by Kytlym dunite zircons, Ural Mts, Russia. *Terra Nova* **2001**, *13*, 407–412. [CrossRef]
87. Wedepohl, K.H. The composition of the continental crust. *Geochim. Cosmochim. Acta* **1995**, *59*, 1217–1232. [CrossRef]
88. Taylor, S.R.; McLennan, S.M. The geochemical evolution of the continental crust. *Rev. Geophys.* **1995**, *33*, 241–265. [CrossRef]
89. Rushmer, T. Partial melting of two amphibolites: Contrasting experimental results under fluid–absent conditions. *Contrib. Mineral Petr.* **1991**, *107*, 41–59. [CrossRef]
90. Rapp, R.P.; Watson, E.B. Dehydration melting of metabasalt at 8–32 kbar: Implications for continental growth and crust–mantle recycling. *J. Petrol.* **1995**, *36*, 891–931. [CrossRef]

91. Singh, J.; Johannes, W. Dehydration melting of tonalites. Part II. Composition of melts and solids. Contrib. *Mineral Petr.* **1996**, *125*, 26–44. [CrossRef]
92. Altherr, R.; Holl, A.; Hegner, E.; Langer, C.; Kreuzer, H. High–potassium, calc–alkaline I–type plutonism in the European Variscides: Northern Vosges (France) and northern Schwarzwald (Germany). *Lithos* **2000**, *50*, 51–73. [CrossRef]
93. Sisson, T.W.; Ratajeski, K.; Hankins, W.B.; Glazner, A.F. Voluminous granitic magmas from common basaltic sources. *Contrib. Mineral Petr.* **2005**, *148*, 635–661. [CrossRef]
94. Jung, S.; Pfänder, J.A. Source composition and melting temperatures of orogenic granitoids: Constraints from CaO/Na_2O, Al_2O_3/TiO_2 and accessory mineral saturation thermometry. *Eur. J. Mineral.* **2007**, *19*, 859–870. [CrossRef]
95. Martin, H.; Smithies, R.H.; Rapp, R.; Moyen, J.F.; Champion, D. An overview of adakite, tonalite–trondhjemite–granodiorite (TTG), and sanukitoid: Relationships and some implications for crustal evolution. *Lithos* **2005**, *79*, 1–24. [CrossRef]
96. Wang, Y.J.; He, H.Y.; Cawood, P.A.; Srithai, B.; Feng, Q.L.; Fan, W.M.; Zhang, Y.Z.; Qian, X. Geochronological, elemental and Sr–Nd–Hf–O isotopic constraints on the petrogenesis of the Triassic post–collisional granitic rocks in NW Thailand and its Paleotethyan implications. *Lithos* **2016**, *266–267*, 264–286. [CrossRef]
97. Sylvester, R.J. Postcollisional strongly peraluminous granites. *Lithos* **1998**, *45*, 29–44. [CrossRef]
98. Wang, Y.J.; Fan, W.M.; Sun, M.; Liang, X.Q.; Zhang, Y.H.; Peng, T.P. Geochronological, geochemical and geothermal constraints on petrogenesis of the Indiosinian peraluminous granites in the South China Block: A case study in the Hunan Province. *Lithos* **2007**, *96*, 475–502. [CrossRef]
99. Wang, Y.J.; Zhang, A.M.; Cawood, P.A.; Fan, W.M.; Xu, J.F.; Zhang, G.W.; Zhang, Y.Z. Geochronological, geochemical and Nd–Hf–Os isotopic fingerprinting of an early Neoproterozoic arc–back–arc system in South China and its accretionary assembly along the margin of Rodinia. *Precambrian Res.* **2013**, *231*, 343–371. [CrossRef]
100. Douce, A.E.; Harris, N. Experimental Constraints on Himalayan Anatexis. *J. Petrol.* **1998**, *39*, 689–710. [CrossRef]
101. Rapp, R.P.; Watson, E.B.; Miller, C.F. Partial melting of amphibolite/eclogite and the origin of Archean trondhjemites and tonalites. *Precambrian Res.* **1991**, *51*, 1–25. [CrossRef]
102. Whalen, J.B.; Currie, K.L.; Chappell, B.W. A–type granites: Geochemical characteristics, discrimination and petrogenesis. Contrib. *Mineral Petr.* **1987**, *95*, 407–419. [CrossRef]
103. Chappell, B.W.; White, A.J.R. I- and S-type Granites in the Lachlan Fold Belt. *Trans. R. Soc. Edinb. Earth Sci.* **1992**, *83*, 1–26.
104. Bonin, B. A–type granites and related rocks: Evolution of a concept, problems and prospects. *Lithos* **2007**, *97*, 1–29. [CrossRef]
105. Whalen, J.B. Geochemistry of an island–arc plutonic suite: The Uasilau–Yau Yau intrusive complex, New Britain, P.N.G. *J. Petrol.* **1985**, *26*, 603–632. [CrossRef]
106. DePaolo, D.J. Trace element and isotopic effects of combined wallrock assimilation and fractional crystallization. *Earth Planet Sci. Lett.* **1981**, *53*, 189–202. [CrossRef]
107. Collins, W.J. Lachlan Fold Belt granitoids: Products of three–component mixing. *Earth Env. Sci. Trans. R.* **1996**, *87*, 171–181.
108. Kemp, A.I.S.; Hawkesworth, C.J.; Foster, G.L.; Paterson, B.A.; Woodhead, J.D.; Hergt, J.M.; Gray, C.M.; Whitehouse, M.J. Magmatic and crustal differentiation history of granitic rocks from Hf–O isotopes in zircon. *Science* **2007**, *315*, 980–983. [CrossRef] [PubMed]
109. Clemens, J.D.; Stevens, G. What controls chemical variation in granitic magmas? *Lithos* **2012**, *134*, 317–329. [CrossRef]
110. Chappell, B.W. Aluminum saturation in I– and S–type granites and the characterization of fractionated haplogranites. *Lithos* **1999**, *46*, 535–551. [CrossRef]
111. Clemens, J.D. S–type granitic magmas–petrogenetic issues, models and evidence. *Earth Sci. Rev.* **2003**, *61*, 1–18. [CrossRef]
112. Villaros, A.; Stevens, G.; Buick, I.S. Tracking S–type granite from source to emplacement: Clues from garnet in the Cape Granite Suite. *Lithos* **2009**, *112*, 217–235. [CrossRef]
113. Chappell, B.W.; White, A.J.R. Two contrasting granite types. *Pac. Geol.* **1974**, *8*, 173–174.
114. Gray, C.M. An isotopic mixing model for the origin of granitic rocks in south–eastern Australia. *Earth Planet Sci. Lett.* **1984**, *70*, 47–60. [CrossRef]
115. Villaros, A.; Buick, I.S.; Stevens, G. Isotopic variations in S–type granites: An inheritance from a heterogeneous source? *Contrib. Mineral Petr.* **2012**, *163*, 243–257. [CrossRef]
116. Chappell, A.; Sanderman, J.; Thomas, M.; Read, A.; Leslie, C. The dynamics of soil redistribution and the implications for soil organic carbon accounting in agricultural south–eastern Australia. *Global Chang. Biol.* **2012**, *18*, 2081–2088. [CrossRef]
117. Zhao, Z.F.; Gao, P.; Zheng, Y.F. The source of Mesozoic granitoids in South China: Integrated geochemical constraints from the Taoshan batholith in the Nanling Range. *Chem. Geol.* **2015**, *395*, 11–26. [CrossRef]
118. King, P.L.; White, A.J.R.; Chappell, B.W.; Allen, C.M. Characterization and origin of aluminous A–type granites from the Lachlan Fold Belt, southeastern Australia. *J. Petrol.* **1997**, *38*, 371–391. [CrossRef]
119. Eby, G.N. The A–type granitoids: A review of their occurrence and chemical characteristics and speculations on their petrogenesis. *Lithos* **1990**, *26*, 115–134. [CrossRef]
120. Zhang, Q.; Ran, H.; Li, C.D. A–type granite: What is the essence? *Acta Petrol. Mineral.* **2012**, *31*, 621–626. (In Chinese with English Abstract)
121. Wang, Q.; Zhao, Z.H.; Xiong, X.L. The Ascertainment of Late–Yanshanian A–type Granite in Tongbai–Dabie Orogenic Belt. *Acta Petrol. Mineral.* **2000**, *19*, 297–306. (In Chinese with English Abstract)
122. Collins, W.J.; Beams, S.D.; White, A.J.R.; Chappell, B.W. Nature and origin of A–type granites with particular reference to southeastern Australia. *Contrib. Mineral. Petr.* **1982**, *80*, 189–200. [CrossRef]

123. Clemens, J.D.; Holloway, J.R.; White, A.J.R. Origin of A–type granites: Experimental constraints. *Am. Mineral.* **1986**, *71*, 317–324.
124. Qu, X.M.; Wang, R.J.; Xin, H.B.; Jiang, J.H.; Chen, H. Age and petrogenesis of A–type granites in the middle segment of the Bangonghu–Nujiang suture, Tibetan plateau. *Lithos* **2012**, *146*, 264–275. [CrossRef]
125. Chappell, B.W.; White, A.J.R. Two contrasting granite types: 25 years later. *J. Geol. Soc. of Aust.* **2001**, *48*, 489–499. [CrossRef]
126. Clemens, J.D.; Stevens, G.; Farina, F. The enigmatic sources of I–type granites: The peritectic connexion. *Lithos* **2011**, *126*, 174–181. [CrossRef]
127. Turner, S.P.; Foden, J.D.; Morrison, R.S. Derivation of some A–type magmas by fractionation of basaltic magma; an example from the Padthaway Ridge, South Australia. *Lithos* **1992**, *28*, 151–179. [CrossRef]
128. Chiaradia, M. Adakite–like magmas from fractional crystallization and melting–assimilation of mafic lower crust (Eocene Macuchi arc, Western Cordillera, Ecuador). *Chem. Geol.* **2009**, *265*, 468–487. [CrossRef]
129. Zorpi, M.J.; Coulon, C.; Orsini, J.B.; Cocirta, C. Magma mingling, zoning and emplacement in calc–alkaline granitoid plutons. *Tectonophysics* **1989**, *157*, 315–329. [CrossRef]
130. Metcalfe, R.V.; Smith, E.I.; Walker, J.D.; Reed, R.C.; Gonzales, D.A. Isotopic disequilibrium among commingled hybrid magmas: Evidence for two–stage magma mixing–commingling processes in the Mt. Perkins pluton, Arizona. *J. Geol.* **1995**, *103*, 509–527. [CrossRef]
131. Jahn, B.M.; Zhang, Z.Q. Archean granulite gneisses from eastern Hebei Province, China: Rare earth geochemistry and tectonic implications. *Contrib. Mineral. Petr.* **1984**, *85*, 224–243. [CrossRef]
132. Baker, M.B.; Hirschmann, M.M.; Ghiorso, M.S.; Stolper, E.M. Compositions of near–solidus peridotite melts from experiments and thermodynamic calculations. *Nature* **1995**, *375*, 308–311. [CrossRef]
133. Valley, J.W.; Lackey, J.S.; Cavosie, A.J.; Clechenko, C.C.; Apicuzza, M.J.; Basei, M.A.S.; Bindeman, I.N.; Ferreira, V.P.; Sial, A.N.; King, E.M.; et al. 4.4 billion years of crustal maturation: Oxygen isotope ratios of magmatic zircon. *Contrib. Mineral Petr.* **2005**, *150*, 561–580. [CrossRef]
134. Castro, A. The off–crust origin of granite batholiths. *Geosci. Front.* **2013**, *5*, 63–75. [CrossRef]
135. Patiño Douce, A.E. Generation of metaluminous A–type granites by low pressure melting of calc–alkaline granitoids. *Geology* **1997**, *25*, 743–746. [CrossRef]
136. Wu, F.Y.; Sun, D.Y.; Li, H.M.; Jahn, B.M.; Wilde, S.A. A–type granites in northeastern China: Age and geochemical constraints on their petrogenesis. *Chem. Geol.* **2002**, *187*, 143–173. [CrossRef]
137. Yang, L.Q.; Deng, J.; Dilek, Y.; Meng, J.Y.; Gao, X.; Santosh, M.; Wang, D.; Yan, H. Melt source and evolution of I–type granitoids in the SE Tibetan Plateau: Late Cretaceous magmatism and mineralization driven by collision–induced transtensional tectonics. *Lithos* **2016**, *245*, 258–273. [CrossRef]
138. Eby, G.N. Chemical subdivision of the A–type granitoids: Petrogenetic and tectonic implications. *Geology* **1992**, *20*, 641–644. [CrossRef]
139. Shellnutt, J.G.; Zhou, M.F. Permian peralkaline, peraluminous and metaluminous A–type granites in the Panxi district, SW China: Their relationship to the Emeishan mantle plume. *Chem. Geol.* **2007**, *243*, 286–316. [CrossRef]
140. Frost, C.D.; Frost, B.R. On Ferroan (A–type) Granitoids: Their compositional variability and modes of origin. *J. Petrol.* **2011**, *52*, 39–53. [CrossRef]
141. Barboni, M.; Bussy, F. Petrogenesis of magmatic albite granites associated to cogenetic A–type granites: Na–rich residual melt extraction from a partially crystallized A–type granite mush. *Lithos* **2013**, *177*, 328–351. [CrossRef]
142. Pankhurst, M.J.; Schaefer, B.F.; Turner, S.P.; Argles, T.; Wade, C.E. The source of A–type magmas in two contrasting settings: U–Pb, Lu–Hf and Re–Os isotopic constraints. *Chem. Geol.* **2013**, *351*, 175–194. [CrossRef]
143. Green, T.H. Significance of Nb/Ta as an indicator of geochemical processes in the crust–mantle system. *Chem. Geol.* **1995**, *120*, 347–359. [CrossRef]
144. Hofmann, A.Q.; Jochum, K.P.; Seufert, M.; White, W.M. Nb and Pb in oceanic basalts: New constraints on mantle evolution. *Earth Planet Sci. Lett.* **1986**, *79*, 33–45. [CrossRef]
145. Frost, C.D.; Frost, B.R. Reduced rapakivi–type granites: The tholeiite connection. *Geology* **1997**, *25*, 647–650. [CrossRef]
146. Clemens, J.D.; Finger, F. Formation of high $\delta^{18}O$ fayalite–bearing A–type granite by high–temperature melting of granulitic metasedimentary rocks, southern China: COMMENT. *Geology* **2012**, *40*, e277. [CrossRef]
147. Qiu, J.S.; Wang, D.Z.; McInners, B.I.A. Geochemistry and petrogenesis of the I– and S–type composite granite masses in the coastal area of Zhejiang and Fujian province. *Acta Petrol. Sin.* **1999**, *15*, 237–246. (In Chinese with English Abstract)
148. Pearce, J.A.; Harris, N.B.; Tindle, A.G. Trace element discrimination diagrams for the tectonic interpretation of granitic rocks. *J. Petrol.* **1984**, *25*, 956–983. [CrossRef]
149. Morrison, G.W. Characteristics and tectonic setting of the shoshonite rock association. *Lithos* **1980**, *13*, 97–108. [CrossRef]
150. Gill, J.B. Orogenic andesites and plate tectonics. *Mineral. Mag.* **1981**, *46*, 277–278.
151. Hao, L.L.; Wang, Q.; Wyman, D.A.; Ma, L.; Wang, J.; Xia, X.P.; Ou, Q. First identification of postcollisional A-type magmatism in the Himalayan-Tibetan orogen. *Geology* **2019**, *47*, 187–190. [CrossRef]
152. Xiao, Y.; Wu, G.H.; Thomas, M.V.; You, L.X. Geochronological and geochemical constraints on Late Cryogenian to Early Ediacaran magmatic rocks on the northern Tarim Craton: Implications for tectonic setting and affinity with Gondwana. *Int. Geol. Rev.* **2019**, *61*, 1–18. [CrossRef]

153. Harris, N.B.W.; Pearce, J.A.; Tindle, A.G. Geochemical characteristics of collision–zone magmatism. *J. Geol. Soc. Lond.* **1986**, *19*, 67–81. [CrossRef]
154. Li, S.; Guilmette, C.; Ding, L.; Xu, Q.; Fu, J.J.; Yue, Y.H. Provenance of Mesozoic clastic rocks within the Bangong–Nujiang suture zone, central Tibet: Implications for the age of the initial Lhasa–Qiangtang collision. *J. Asian Earth Sci.* **2017**, *147*, 469–484. [CrossRef]
155. Thompson, A.B. Some time–space relationships for crustal melting and granitic intrusion at various depths. *Geol. Soc. London Spec. Publ.* **1999**, *168*, 7–25. [CrossRef]
156. Schulmann, K.; Jezek, J. Some remarks on fabric overprints and constrictional AMS fabrics in igneous rocks. *Int. J. Earth Sci.* **2012**, *101*, 705–714. [CrossRef]
157. von Blanckenburg, F.; Davies, J.H. Slab breakoff: A model for syncollisional magmatism and tectonics in the Alps. *Tectonics* **1995**, *14*, 120–131. [CrossRef]
158. Wong, T.F.; Ko, S.C.; Olgaard, D. Generation and maintenance of pore pressure excess in a dehydrating system: 2. Theoretical analysis. *J. Geophys. Res.* **1997**, *102*, 841–852. [CrossRef]
159. Barbarin, B. A review of the relationships between granitoid types, their origins and their geodynamic environments. *Lithos* **1999**, *46*, 605–626. [CrossRef]
160. Collins, W.J.; Richards, S.W. Geodynamic significance of S–type granites in circum–Pacific orogens. *Geology* **2008**, *36*, 559–562. [CrossRef]
161. Yuan, C.; Sun, M.; Wilde, S.; Xiao, W.J.; Xu, Y.G.; Long, X.P.; Zhao, G.C. Postcollisional plutons in the Balikun area, East Chinese Tianshan: Evolving magmatism in response to extension and slab break–off. *Lithos* **2010**, *119*, 269–288. [CrossRef]